National Library of Canada
Acquisitions and Bibliographic Services Branch
395 Wellington Street
Ottawa, Ontario
K1A 0N4

Bibliothèque nationale du Canada
Direction des acquisitions et des services bibliographiques
395, rue Wellington
Ottawa (Ontario)
K1A 0N4

Your file Votre référence

Our file Notre référence

NOTICE

The quality of this microform is heavily dependent upon the quality of the original thesis submitted for microfilming. Every effort has been made to ensure the highest quality of reproduction possible.

If pages are missing, contact the university which granted the degree.

Some pages may have indistinct print especially if the original pages were typed with a poor typewriter ribbon or if the university sent us an inferior photocopy.

Reproduction in full or in part of this microform is governed by the Canadian Copyright Act, R.S.C. 1970, c. C-30, and subsequent amendments.

AVIS

La qualité de cette microforme dépend grandement de la qualité de la thèse soumise au microfilmage. Nous avons tout fait pour assurer une qualité supérieure de reproduction.

S'il manque des pages, veuillez communiquer avec l'université qui a conféré le grade.

La qualité d'impression de certaines pages peut laisser à désirer, surtout si les pages originales ont été dactylographiées à l'aide d'un ruban usé ou si l'université nous a fait parvenir une photocopie de qualité inférieure.

La reproduction, même partielle, de cette microforme est soumise à la Loi canadienne sur le droit d'auteur, SRC 1970, c. C-30, et ses amendements subséquents.

Canada

UNIVERSITY OF ALBERTA

INVESTIGATION OF BACKSCATTERED LIGHT FROM FIBRE MICROBENDS

by

LUTFUL KABIR KHAN

A thesis submitted to the Faculty of Graduate Studies and Research in partial fulfillment of the requirements for the degree of MASTER OF SCIENCE.

DEPARTMENT OF ELECTRICAL ENGINEERING

Edmonton, Alberta
FALL 1992

National Library of Canada
Bibliothèque nationale du Canada

Canadian Theses Service
Service des thèses canadiennes

Ottawa, Canada
K1A 0N4

The author has granted an irrevocable non-exclusive licence allowing the National Library of Canada to reproduce, loan, distribute or sell copies of his/her thesis by any means and in any form or format, making this thesis available to interested persons.

The author retains ownership of the copyright in his/her thesis. Neither the thesis nor substantial extracts from it may be printed or otherwise reproduced without his/her permission.

L'auteur a accordé une licence irrévocable et non exclusive permettant à la Bibliothèque nationale du Canada de reproduire, prêter, distribuer ou vendre des copies de sa thèse de quelque manière et sous quelque forme que ce soit pour mettre des exemplaires de cette thèse à la disposition des personnes intéressées.

L'auteur conserve la propriété du droit d'auteur qui protège sa thèse. Ni la thèse ni des extraits substantiels de celle-ci ne doivent être imprimés ou autrement reproduits sans son autorisation.

ISBN 0-315-77279-4

Canada

UNIVERSITY OF ALBERTA

RELEASE FORM

NAME OF AUTHOR:	Lutful Kabir Khan
TITLE OF THESIS:	Investigation of Backscattered Light From Fibre Microbends
DEGREE:	Master of Science
YEAR THIS DEGREE GRANTED:	Fall, 1992

Permission is hereby granted to the University of Alberta Library to reproduce single copies of this thesis and to lend or sell such copies for private, scholarly or scientific research purposes only.

The author reserves all other publication and other rights in association with the copyright in the thesis, and except as hereinbefore provided neither the thesis nor any substantial portion thereof may be printed or otherwise reproduced in any material form whatever without the author's prior written permission.

Md Lutful Kabir Khan

62, Sikkatuly Lane, Nazirabazar
Dhaka 1000
BANGLADESH

Date: July 9, 1992

UNIVERSITY OF ALBERTA

FACULTY OF GRADUATE STUDIES AND RESEARCH

The undersigned certify that they have read, and recommend to the Faculty of Graduate Studies and Research for acceptance, a thesis entitled INVESTIGATION OF BACKSCATTERED LIGHT FROM FIBRE MICROBENDS submitted by LUTFUL KABIR KHAN in partial fulfillment of the requirements for the degree of MASTER OF SCIENCE.

J. McMullin (Co-Supervisor)

M. Cervenan (Co-Supervisor)

R. MacDonald (Committee Member)

W. Lipsett (Committee Member)

Not Applicable

R. Lawson (Committee Chair)

Date: July 6, 1992.

ABSTRACT

The phenomenon of backscattering enhancement from optical fibre microbends was investigated with the aid of a photon-counting optical time domain reflectometer. It was found that a single microbend of the fibre, placed on an elastic foundation, produced more enhancement of the backscattered light level for a given loss than did periodic microbends. The main contributor to the backscattering enhancement for a jacketed optical fibre was found to be the jacket itself. In case of a fibre stripped of its jacket, any scattering medium surrounding the fibre was found to cause some backscattering enhancement.

The peaks of the enhanced backscattering were found to be easier to detect than the Rayleigh backscattering drop due to loss at the microbend. Under suitable conditions, the peak of the enhanced backscattering could be 15 dB higher than the Rayleigh backscattering level before the microbend. The use of backscattering enhancement was found to be suitable for distributed optical fibre sensors to measure force and displacement.

ACKNOWLEDGEMENTS

I sincerely appreciate the guidance and encouragement provided to me by Dr. Jim McMullin and Dr. Martin Cervenan throughout the project. I thank the Laser Institute for providing the facilities and financial support to conduct the research.

I recognize the invaluable support of my wife, Marika, who helped me organize the bibliography and the figures. She was most considerate and reassuring during the writing of the thesis.

TABLE OF CONTENTS

Introduction 1

Propagation and Attenuation 5

2.1 Modes of propagation 5

2.2 Optical power flow 8

2.3 Attenuation 10

2.4 Applied bends & microbends 12

Rayleigh Scattering 17

3.1 The physical basis of Rayleigh scattering 17

3.2 Calculating the Rayleigh coefficient 21

3.3 Calculating α_R from loss data 22

The Backscattered Trace 24

4.1 Theory of the backscattered trace 25

4.2 Calculated trace for the test fibre 28

4.3 Backscattering from perturbed fibres 30

4.4 Backscattered trace from bends 32

Optical Time Domain Reflectometry 34

5.1 Designing an OTDR 34

5.2 Sensitivity and resolution 36

5.3 A photon counting OTDR 38

5.4 Operation of the detector 39

The Experiments 46

6.1 Software design 47

6.2 The effects studied 48

Analysis of Results 54
7.1 Periodic microbends 55
7.2 Single bends on an elastic foundation 57
7.2.1 Effect of different surface types 58
7.2.2 Effect of the bend profile 61
7.2.3 Hysteresis effect of the elastic foundation 64
7.2.4 Effect of the removal of the fibre jacket 65
7.2.5 Overall comparison 67
7.2.6 Investigation of bends in series 68

Conclusions 99

Bibliography 102

LIST OF TABLES

Table 2.1 Specifications of the Corguide® optical fibre 8

Table 3.1 Physical parameters for fused silica 21

Table 3.2 Calculation of α_R from loss data 23

Table 4.1 Backscatter parameters of the test fibre 29

Table 7.1 Effect of the surface on which the fibre is placed 60

LIST OF FIGURES

Figure 2.1 The curvature spectrum at two different modal separations for a sinusoidal microbend 15

Figure 2.2 The curvature spectrum plotted against distortion amplitude for various number of periods 16

Figure 4.1 The backscatter trace for a short 1 picoJoule pulse from three different intervals 33

Figure 5.1 The Optical Time Domain Reflectometer 42

Figure 5.2 The probability of exactly none, one, or more than one photons arriving at the detector for a given average level of arriving photons 43

Figure 5.3 The probability of an avalanche breakdown when an average of n photons are arriving at the APD 44

Figure 5.4 The linearity of the probability function of avalanche breakdown for less than one photon per interval 45

Figure 6.1 The bender instrument 50

Figure 6.2 Flow diagram of 'SenLab' software 51

Figure 6.3 Setup for periodic bending experiments 52

Figure 6.4 Setup for single bend experiments 53

Figure 7.1 Flow diagram of data analysis software 70

Figure 7.2 Backscatter enhancement from periodic microbends 71

Figure 7.3 Peaks of the enhanced backscattering at various microbending amplitudes 72

Figure 7.4 Losses produced by periodic microbending 73

Figure 7.5 Comparison between the loss and peak levels produced by the same microbending distortion 74

Figure 7.6 The peaks produced by resting the fibre on two different paper surfaces on a foam foundation 75

Figure 7.7 The (power meter) losses due to bending the fibre on two different surfaces 76

Figure 7.8 The (OTDR) losses due to bending the fibre on two different surfaces 76

Figure 7.9 Comparison of the peaks against the losses due to bending the fibre on two different surfaces 77

Figure 7.10 Bend shapes on different surfaces 78

Figure 7.11 Comparison of the shape of the bend on two different surfaces 79

Figure 7.12 Photographs of the bend profiles for increasing bender displacements 80

Figure 7.13 The peaks produced by two different rod diameters 81

Figure 7.14 The (power meter) losses produced by two different rod diameters 82

Figure 7.15 The (OTDR) losses produced by two different rod diameters 82

Figure 7.16 Comparison of the peaks against losses for two different rod diameters 83

Figure 7.17 The profiles obtained for two different bender displacements 84

Figure 7.18 The relationship of the FWHM of the bend profile to the bender displacement 85

Figure 7.19 The relationship of the peak and loss to the FWHM of the bend profile 85

Figure 7.20 A probable mechanism for the backscatter enhancement 86

Figure 7.21 Observation of a 'hysteresis effect' on the peak when displacement is increased to a maximum and gradually decreased 87

Figure 7.22 Observation of a 'hysteresis effect' on the loss when displacement is increased to a maximum and gradually decreased 87

Figure 7.23 Difference in the shape of the fibre for the same displacement, but when the bender movement was in opposite directions 88

Figure 7.24 The peaks produced at different displacements for jacketed and bare fibres 89

Figure 7.25 The (power meter) losses at different displacements for jacketed and bare fibres.....90

Figure 7.26 The (OTDR) losses at different displacements for jacketed and bare fibres.....90

Figure 7.27 Comparison of the peaks against the losses for jacketed and bare fibres.....91

Figure 7.28 Bend profiles for a fibre whose jacket has been removed.....92

Figure 7.29 The effect of two different metallic sprays on the peak levels for a bare fiber.....93

Figure 7.30 The effect of two different metallic sprays on the loss levels for a bare fiber.....93

Figure 7.31 The remarkable difference in the peak and loss levels for fibres with and without a jacket for a similar bend profile.....94

Figure 7.32 Overall comparison between the peak and loss levels for the experiments performed.....95

Figure 7.33 The backscattering trace showing enhancement peaks from three locations pressed by equal forces of 200 gm-wt.....96

Figure 7.34 The effect on the backscattered trace after a force change at one location.....97

Figure 7.35 The backscattered trace expressed in decibels above or below the initial level.....98

Figure 7.36 The smoothed backscattered trace.....98

LIST OF SYMBOLS AND ABBREVIATIONS

a	radius of the core
α_P	attenuation coefficient due to perturbation
APD	avalanche photodiodes
α_R	Rayleigh attenuation coefficient
$a_r(t)$; $a_r(z)$	Rayleigh attenuation function
α_T	Total attenuation in nepers or dBs per unit distance
B(t); B(z)	backscatter trace
β_m	propagation constant
β_{pq}	propagation constant
B_T	isothermal compressibility
BW	bandwidth
δ	amplitude of distortion
d(z)	perturbation function
D, Λ	correlation length
$\delta\beta$	difference between the propagation constants
DOFS	Distributed Optical Fibre Sensors
$\Phi(\Omega)$	perturbation spectrum
f(z)	geometry of the bent fibre
FWHM	pulse full width at half maximum
GPIB	a general purpose parallel bus (IEEE-488)
η	photon counting quantum efficiency of the APD
$h\nu$	energy of a photon
$k_0 = 2\pi/\lambda$	free space wavelength

K_B	Boltzman constant
Λ	distortion wavelength
MPD	Modal Power Distribution
N	total number of guided modes
n_0	average refractive index
$n_0(x,y,z)$	refractive index
n_1	core index
n_2	cladding index
NA	numerical aperture
NEP	noise equivalent power
OTDR	Optical Time Domain Reflectometry
p	photoelastic coefficient
P_0	peak laser power
PDR	Photon Detection Ratio
$P_i(t)$	input pulse
$P_{in}(R)$	MPD at the input end of the fibre
R	normalized mode parameter
$\boldsymbol{R}$	Reflection Coefficient
R_c	curvature of the bend
T	absolute or fictive temperature
τ	width of pulse
T_{on}	interval in which APD is active
V	normalized frequency parameter
v	group velocity of light in medium
Ω	spatial frequency
WKB	Wentzel-Kramers-Brillouin approximation

Chapter 1

INTRODUCTION

Telecommunication remains the principal application for optical-fibre technology due to the large bandwidth, lightweight cables, small crosstalk, and relative immunity from electromagnetic interference. However, the optical fibre is getting increased acceptance as a component for sensor systems.

The same qualities that make optical fibre technology desirable for communication also extend to sensors. In addition, novel system architectures, such as sensor systems that will enable continuous monitoring of the magnitude and spatial distribution of multiple physical parameters, are theoretically possible using optical-fibre technology. System requirements for these Distributed Optical Fibre Sensors (DOFS) have been investigated, and sensor systems have been implemented to measure spatial distributions of temperature, stress, pressure, electromagnetic fields, and chemicals[1,2].

One method used for investigating distributed fibre sensors is Optical Time Domain Reflectometry (OTDR), which is analogous to RADAR but in the optical domain. OTDR, originally developed for the assessment of telecommunication cables, allows the monitoring of the spatial distribution of backscattered and reflected light from a long length of fibre. To investigate a fibre by OTDR, a short laser pulse is launched into the fibre, and the returning lightwave is detected by a sensitive photodetector. The

result is the backscatter trace, a time function of the level of light returning from locations in the fibre.

The backscatter trace is a signature of the passage of light in an optical fibre. The location, nature and magnitude of any parameter which perturbs this passage may be deduced from this signature. Hence, the backscattering technique offers an unique opportunity to develop fully distributed sensors.

The benefits of distributed optical fibre sensors over traditional electronic sensor arrays are enormous. Electronic interrogation of traditional sensor arrays usually require that each individual sensor have a power source and circuitry for processing of the sensor data for transmission. There is also a need for circuitry to distinguish between the sensors in an array. Precautions need to be taken to ensure that the electronic data are not unduly corrupted by interference. The fiber sensor can be configured so that all the interrogation and processing takes place at one end of the fiber kilometers away from the sensing environment. The sensor elements can be made totally passive with no power sources or processing circuitry required. In addition, it is possible to have truly continuous spatial sensing with arbitrarily small distance resolution using suitable OTDR equipment.

Conventional and photon counting OTDRs are commercially available, and are less expensive and more rugged than specialized equipment such as the Coherent or Raman OTDR. Distributed sensor systems have been implemented using conventional OTDRs and microbending sensor elements[2-4]. Microbending sensors impose periodic

small-radius bends on the fibre, and produce excess attenuation whose location and magnitude can be related to the physical effect producing the distortion. A wide variety of physical parameters have been measured using these types of sensors[5-9].

When multiple microbending sensors are serially placed to form a quasi-distributed system, the backscattered trace after a few elements may drop to very low levels making accurate determination of the loss difficult. Photon counting OTDRs provide more allowance for the loss budget, but the noise level of the backscattered trace reduces accuracy. Sensors that depend on attenuation of the backscattered trace may not be an ideal choice for a distributed optical fibre sensor system.

Enhancement of the backscatter trace has been observed from periodic microbend sensors[3], and small radius loops[10], but not studied in detail. In both these cases, the probable cause of the backscatter enhancement was not mentioned. Since the ideal sensor for distributed sensing should have low transmission loss to allow many sensors in series, yet provide an easily measurable change in the signal level due to the external parameter, sensors based on enhancement of the backscattered light merit further study. Further investigation of the backscattered trace at fibre microbends is required to develop such a sensor element.

This project was undertaken to reproduce the enhancement of the backscatter trace for various microbend geometries and to investigate the probable cause using an advanced photon counting OTDR that could detect extremely small levels of backscattered light. One of the objectives was to

develop sensor elements that make use of the enhanced backscattering from fibre microbends.

The basic theory of optical wave propagation and attenuation, as it pertains to the fibre under investigation, is presented in Chapter 2. The Rayleigh scattering phenomenon and the resulting backscatter trace are studied in some detail in Chapters 3 and 4 to facilitate a better understanding of the probable causes of the enhancement in the backscatter trace. A brief study of the OTDR and photon counting is undertaken in Chapter 5 to help analyze the experimental data.

Chapters 6 to 8 describe the experimental setup used to investigate the backscattering from microbends, the results of many experiments, the conclusions reached, and the implications for the application of this phenomenon to sensor technology.

Chapter 2

PROPAGATION AND ATTENUATION

Optical power is transferred through a fibre by the propagation of electromagnetic waves with frequencies in the range of 200-500 terahertz. The waves form distinct electromagnetic field patterns or "modes" due to the geometrical symmetry and boundary conditions of the waveguide. Each of these modes is characterized by a propagation constant in the direction of optical power transfer. These propagation constants determine whether a mode will be guided through the fibre core, or if it will radiate power away from the core.

2.1 MODES OF PROPAGATION

Excellent treatments of the solution of Maxwell's equations for optical waveguides can be found in textbooks. Only the simplified results for parabolic index fibres are presented here. The relative difference, Δ, between the core index, n_1, and the cladding index, n_2, is so small in modern communication fibres that we can write the index profile as

$$n(r) \approx n_1 [\, 1 - \Delta\, (r/a)^2 \,], \quad \text{for } r < a, \text{ and} \qquad [2.1a]$$

$$n(r) \approx n_1 [\, 1 - \Delta \,], \quad \text{for } r \geq a\,, \qquad [2.1b]$$

where a is the radius of the core. The total number of guided modes of this fibre can be determined from V, the normalized frequency parameter[11],

$$V = k_0\, a\, (NA), \qquad [2.2]$$

where $k_0 = 2\pi/\lambda$ is the free space wavelength, and NA is the numerical aperture of the fibre,

$$NA = \sqrt{n_1^2 - n_2^2}\,. \qquad [2.3]$$

The total number of guided modes is given by

$$N = \frac{V^2}{4} \qquad [2.4]$$

for a parabolic index fibre.

Each of these modes is characterized by a propagation constant, β_{pq}, where q represents the number of radial zeros, and p represents half the number of angular zeros of the electromagetic field distributions which are essentially transverse and of the form[11]

$$\Psi(r,\phi,z) = F(r)\, e^{\pm jp\phi}\, e^{-j\beta_{pq}z}. \qquad [2.5]$$

F(r) has been determined theoretically[12] but approximations such as the WKB method provide an easier way of calculating the propagation constants.

It can been shown that the total number of guided modes, N, with propagation constants, β_{pq}, degenerate or coalesce to only $\sqrt{N}$ mode groups[12,13]. Each of these mode groups have a unique propagation constant, β_m, given by

$$\beta_m = n_1 k_0 \left[1 - \Delta \frac{m}{M}\right], \qquad [2.6a]$$

where,

$$m = 2p + q + 1, \text{ and} \qquad [2.6b]$$

$$M = \sqrt{N} = \frac{1}{2} k_0 \, a \, (NA). \qquad [2.6c]$$

In Equation 2.6, m represents the mode group number, and M is the total number of degenerate mode groups.

The values of β_m determine the nature of the electromagnetic fields in the fibre. The electromagnetic fields are confined to the core region and

propagate down the fibre when β_m is real and falls within[12]

$$n_1 k_0 = |\beta_1| > |\beta_2| > \ldots > |\beta_M| = n_2 k_0. \qquad [2.7]$$

The negative values of β_m, which indicate propagation in the negative z direction, are only to be used when there is a mechanism to excite modes. It can be determined that the difference between the propagation constants of the guided modes,

$$\delta\beta = \frac{\sqrt{2\Delta}}{a}, \qquad [2.8]$$

is a constant for parabolic index fibres. When β is real and in the range

$$n_2 k_0 > \beta > -n_2 k_0, \qquad [2.9]$$

the modes are not guided and exist in the core, cladding, and beyond. These "radiation modes" carry power away from the core and provide a loss mechanism for any optical waveguides. When β is complex and the real and imaginary components satisfy the conditions[12]

$$n_2 k_0 > \mathbf{Re}(\beta) > -n_2 k_0 \text{ and } \mathbf{Im}(\beta) > 0, \qquad [2.10]$$

the resulting "leaky modes" are always lossy and tunnel power away from the core, but some of these may be partially guided for significant distances along the propagation axis[11]. Any optical field propagating in the fibre can be expressed as a linear superposition of the guided, leaky and radiation modes.

The test fibre used in the experiments has the specifications given in Table 2.1. The index profile is essentially parabolic. The values for V, N M, $\delta\beta$, and the range of values for β have been calculated using Equations 2.1 to 2.9.

Table 2.1 Specifications of the Corguide® optical fibre[26]

Core Diameter	50 ± 3 μm
Cladding Diameter	125 ± 2.0 μm
Core Index	1.4655 at 850 nm
Numerical Aperture	0.200 ± 0.015
Calculated Results	
$n_2 = 1.4517$ [2.1]	$\Delta = 0.0093$ [2.1]
$k_0 = 7.4\ \mu m^{-1}$	$V = 37$ [2.2]
$N = 342$ [2.4]	$M = 18$ [2.6]
$\delta\beta = 0.0055\ \mu m^{-1}$ [2.8]	$10.74\ \mu m^{-1} < \beta_{guided} < 10.84\ \mu m^{-1}$ [2.9]

2.2 OPTICAL POWER FLOW

Since the electromagnetic field distributions of the parabolic index fibre discussed above are nearly transverse, the optical power in the guided modes flows along the propagation axis only and does not vary with z when there is no attenuation present. The radiation modes will carry power away from the core at angles determined by the propagation constants.

The distribution and coupling of power between the modes is of greater concern than the power in any single mode. The Modal Power Distribution (MPD) function can be determined from the optical source

characteristics and the launching conditions. It has been experimentally determined that for AlGaAs semiconductor striped lasers coupled to a parabolic index fibre, the launched MPD takes the form[14]

$$p_{in}(R) = P_0 (1-R) , \qquad [2.11]$$

where P_0 is the peak laser power coupled into the fibre and R is a normalized mode parameter defined as

$$R = \left[\frac{1-(\beta/n_1 k_0)^2}{2\Delta} \right]^{1/2} . \qquad [2.12]$$

The total power at a cross section of the fibre is the integral of the MPD for all guided and radiation modes over the core region of the fibre. For a lossless and geometrically perfect waveguide, the power distribution will not change over the length of the fibre and the power transferred across any cross section of the fibre will be given by[14,15]

$$P = \int_0^1 P_{in}(R)\, N(R)\, dR , \qquad [2.13]$$

where $P_{in}(R)$ is the MPD at the input end of the fibre, and N(R) is the number of degenerate modes identified by the same mode parameter, R. For parabolic index fibres,

$$N(R) = V^2 R^3 . \qquad [2.14]$$

The parameter V is defined in Equation 2.2. When there is attenuation present in the fibre, the power at any cross section at location z of the fibre will be given by

$$P(z) = V^2 \int_0^1 p_{in}(R) \exp\left[-\int_0^z \alpha(R,z)dz \right] R^3 dR . \qquad [2.15]$$

When $\alpha(R,z)$, the attenuation function, is dependent on the mode parameter R, the fibre is said to have Differential Mode Attenuation (DMA).

2.3 ATTENUATION

Attenuation in an optical fibre may be expressed by the general relationship

$$\alpha(\lambda,z) = \alpha_A(\lambda) + \alpha_R(\lambda) + \alpha_P + \alpha_B(\lambda,z)\,, \qquad [2.16]$$

where the components describe the effect and dependence of absorption, Rayleigh scattering, scattering due to perturbations of the fibre parameters, and bending of the fibre axis.

Material absorption in pure silica, which occurs due to the conversion of photons into phonons, is smaller than 1 dB/km in the 800 to 1500 nm wavelength regions[13]. At ultraviolet and far infrared regions, it is enhanced significantly, and $\alpha_A(\lambda)$ can be described as exponential functions of the wavelength. Dopant materials and impurity ions also contribute to the absorption term. The effect of the hydroxyl ion (OH^-), is pronounced within narrow bands at 1.25 and 1.39 μm wavelengths.

Rayleigh scattering is due to the small scale fluctuations in the structure of the silica, the dopant and other impurity molecules. The $\alpha_R(\lambda)$ term has a λ^{-4} dependence which accounts for the preference of longer wavelengths ($\lambda > 0.8$ μm) for optical communication. A detailed study of the Rayleigh scattering process will be undertaken in Chapter 3.

Real fibres will have imperfections such as index profile variation, core diameter fluctuation, core ellipticity deformation, and random bends of the fibre axis. The result of these perturbations is the transfer of power from one mode to another. Since some of the power of guided modes is converted to radiation modes, the net effect is attenuation. These

imperfections are mostly random in nature, and have varying z dependence for different fibres from the same manufacturing process. However, due to the special statistical nature of these perturbations, a correlation function, $R_p(\zeta)$, can be defined as the ensemble average of the perturbation functions, $\langle f(z)\, f(z+\zeta)\rangle$. The distance over which this function has significant amplitudes, called the correlation length, Λ, provides an important measure of the average distance over which a perturbation is effective. The attenuation coefficient, α_p, is proportional to the spatial frequency spectrum of the correlation function $R_p(\zeta)$, or the perturbation spectrum, $\Phi(\Omega)$.

An analytical study of $\Phi(\Omega)$ yielded several important results[16]. Power coupling between two modes β_{m1} and β_{m2} can occur only if there is a spatial frequency component with a finite and non-zero amplitude in the spectrum which meets the condition,

$$0 < \Phi(\beta_{m1}-\beta_{m2}) < \infty . \qquad [2.17]$$

For most of these random perturbations, there is also a cutoff spatial frequency, Ω_c, beyond which the spectrum $\Phi(\Omega)$ does not have any components. Coupling between modes with widely separated propagation constants will take place only if

$$\left|\beta_{m1} - \beta_{m2}\right| < \Omega_c . \qquad [2.18]$$

The correlation length of the perturbation is inversely proportional to this cutoff frequency,

$$\Omega_c \propto 2\pi(\Lambda^{-1}). \qquad [2.19]$$

The summary effect of the conditions imposed in Equations 2.17-2.19 is that for statistical parameter fluctuations and random microbends of the

fibre axis, the power is coupled strongly between adjacent modes. Loss of power occurs when some of the power from modes with large R parameters is coupled into radiation modes. The attenuation coefficient can be calculated from a knowledge of the correlation length and the spatial frequency spectrum of the perturbation function.

Since a parabolic index fibre has a constant separation between the propagation constants, $\delta\beta$, equal to $\sqrt{2\Delta}/a$, coupling will occur only when the perturbation spectrum has significant components at spatial frequencies corresponding to multiples of $2\pi/\delta\beta$.

2.4 APPLIED BENDS & MICROBENDS

The attenuation coefficient of a constant curvature bend is constant along the bent region of the fibre for a particular mode of propagation and may be expressed by the generalized formula[13],

$$\alpha_B = \frac{F}{\sqrt{R_c}}\, e^{-G R_c}, \qquad [2.20]$$

where R_c is the curvature of the bend, and F and G are functions of various fibre parameters and the propagation constants. There is also a transition loss associated with the abrupt change of the radius of curvature at any junctions. The guided modes of one segment couple power into the radiated modes of the next. For gentle bends of much larger radius than that of the fibre, some of the radiated power may couple back to the guided modes[16].

When the radius of curvature is not a constant and there are many modes propagating in the fibre, it is easier to define a curvature spectrum or a displacement spectrum, similar to the perturbation spectrum

described in Section 2.3,

$$\Phi(\Omega) = 1/(L) \left| \int_{-L/2}^{L/2} f(z) \exp [-j\Omega z] dz \right|^2 , \qquad [2.21]$$

where f(z) describes the geometry of the bent fibre in the interval between -L/2 and L/2.

When a sinusoidal microbend is applied to a parabolic fibre, the curvature spectrum is approximated by [17,18]

$$\Phi(\Omega) = \delta^2 (L/2) \operatorname{sinc}^2 [L (2\pi/\Lambda - \Omega) / \pi] \qquad [2.22]$$

for a distortion of wavelength Λ and amplitude of δ applied over a section of length L. Since power coupling can occur only for

$$\Omega = n \, \delta\beta , \qquad [2.23]$$

where n is an integer that indicates the separation between the mode groups that can be coupled, it can be deduced that the most attenuation will occur when the distortion wavelength is

$$\Lambda = \frac{2\pi}{n \, \delta\beta} , \qquad [2.24]$$

and power from the n highest modes will be lost by coupling to the radiation modes. For the test fibre, the ideal distortion wavelength for maximum attenuation is $\frac{1.14}{n}$ mm. If n is chosen to be 3 or larger, the wavelength will be smaller than the diameter of the fibre, and there may be mechanical difficulties in creating a sinusoidal distortion of the core.

Since the spectrum $\Phi(\Omega)$ is a continuous function, even for a choice of $\Lambda = \frac{2\pi}{\delta\beta}$, there may be non-zero components at $n\delta\beta$, given by

$$\Phi(n \, \delta\beta) \propto \operatorname{sinc}^2 [2 (1-n) L / \Lambda] . \qquad [2.25]$$

From a table of the sinc squared function, we see that the maximum loss we can achieve by power transfer between the second highest guided mode

to the radiation modes is only 1.6% of the value of the loss produced by the highest guided mode. This condition is met when L is chosen to be 1.25 periods long, and the two highest modes carry equal power. For a larger number of periods, the power coupling takes place essentially between adjacent modes only.

The distortion wavelength may be made into multiples of $(2\pi/\delta\beta)$ with a similar reduction in attenuation due to the sinc squared function. However, the larger Λ will make possible larger values for δ, the distortion amplitude and provide higher losses.

The induced attenuation due to the microbending is directly proportional to $\Phi(\delta\beta)$, the value of the curvature spectrum at the spatial frequency of the mode separation[19]. This function is plotted against the distortion wavelength Λ, and the distortion amplitude δ in Figures 2.1 and 2.2.

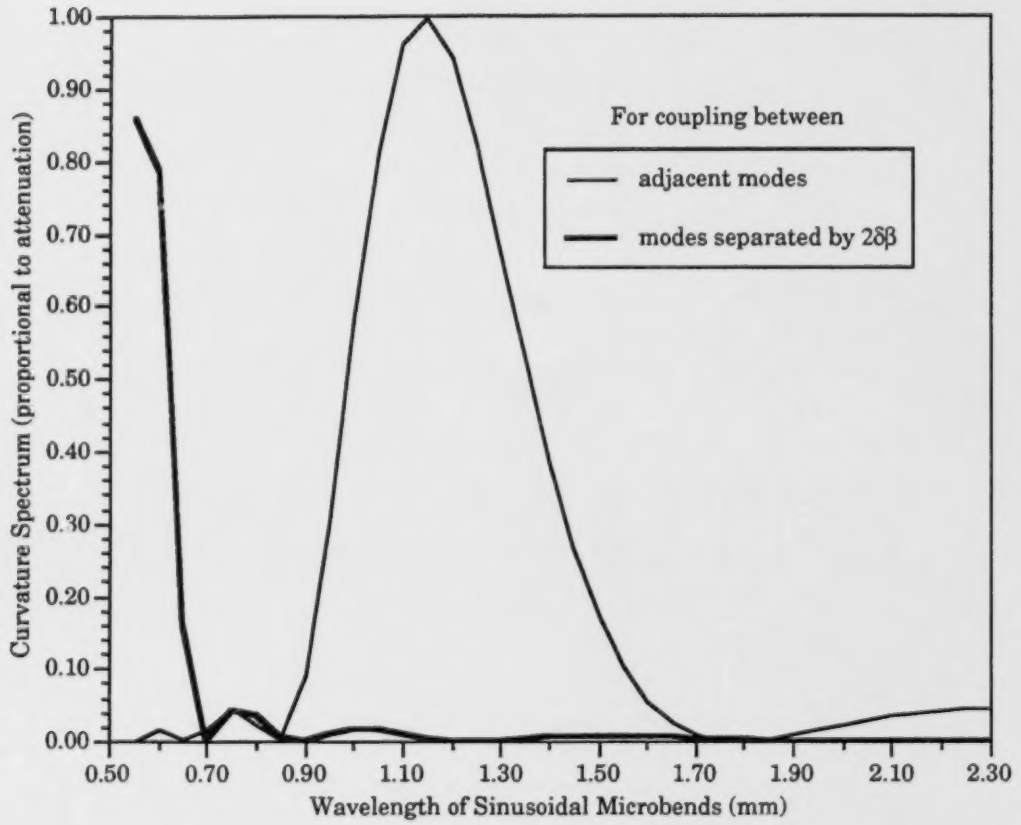

Figure 2.1 The curvature spectrum at two different modal separations for a sinusoidal microbend. ($\delta\beta$ = 5.5 mm^{-1}; 4 periods.)

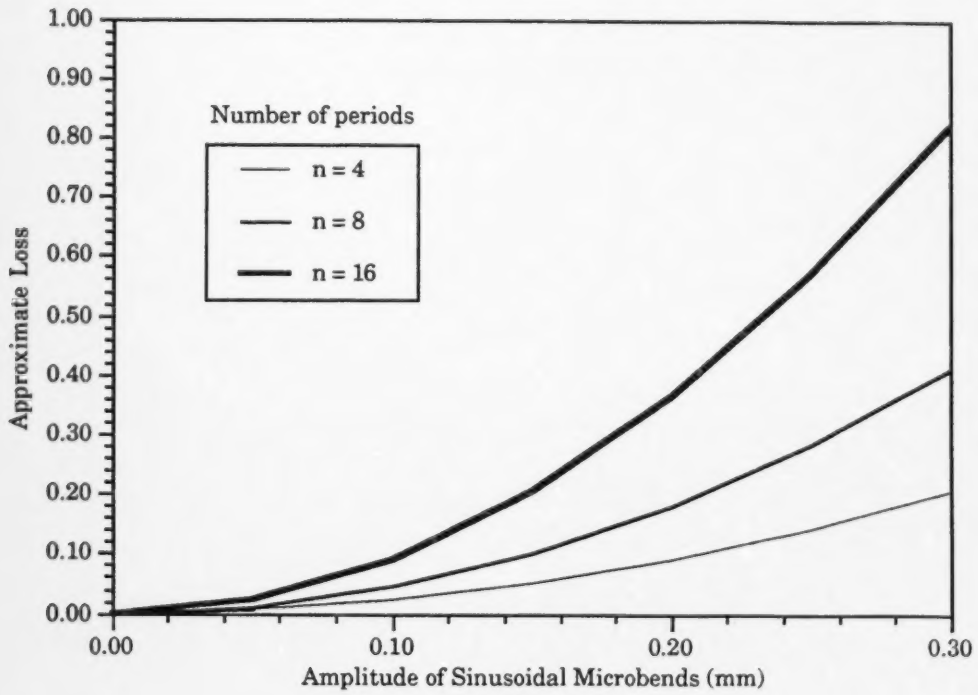

Figure 2.2 The curvature spectrum function plotted against distortion amplitude for various number of periods. (Λ = 1.14 mm.)

Chapter 3

RAYLEIGH SCATTERING

Rayleigh scattering contributes to optical attenuation in any transmission medium where the molecules present microscopic scattering centres to the propagating electromagnetic waves. A brief and general description of the theoretical basis of Rayleigh scattering and some calculations for commercially available fibres are presented in this section.

In the early days of fibre optics, chemical impurities and physical defects were the most significant contributors to the attenuation in optical fibres. When the optical fibre was first suggested as a long distance transmission medium in 1966, the best fibres then available presented greater than 1000 dB/km losses[11] — mainly due to random geometric perturbations and large scale impurities introduced during the fibre drawing process.

As a result of better understanding of the effects of perturbations, fibre manufacturing processes were continualy refined, and fibres with less than 10 dB/km attenuation were fabricated in the early seventies to make their use in communication a reality. Today, optical fibres with less than 0.2 dB/km losses are commercially available. These levels are close to the attenuation due to Rayleigh scattering only for the fibre materials.

3.1 THE PHYSICAL BASIS OF RAYLEIGH SCATTERING

Rayleigh scattering is caused by the density fluctuations in an optical medium. These fluctuations occur on a scale smaller than the wavelength

of light. Detailed theoretical study of the scattering process caused by the refractive index fluctuations has been performed[20] for a plane wave incident on a general optical medium.

Starting from Maxwell's equations for fields in a perfectly homogeneous dielectric space with refractive index $n_0(x,y,z)$, a small index perturbation,

$$n(x,y,z)=n_0(x,y,z)+\delta n(x,y,z)\ , \qquad [3.1]$$

is introduced to account for the fluctuations. Higher order effects can be neglected for $\delta n << n_0$ and the electromagnetic field can be expressed as the sum of the field due to the perfect index distribution plus a perturbed field.

The refractive index perturbation is assumed to be significantly different from zero only inside finite volumes, and the index fluctuations between many such volumes are predicted to follow a stationary random process. The power that is radiated away by the scattering volumes can be calculated from the Poynting vector of the perturbed fields. The attenuation coefficient can then be obtained by dividing the total power lost per unit length, by the power carried in the incident waves.

Marcuse presents the following general formula for the power loss coefficient of Rayleigh scattering:[20]

$$\alpha_R=\frac{32\,\pi^3}{3}\,\frac{n_0^2}{\lambda^4}\,\langle\delta n^2\rangle\,D^3\ . \qquad [3.2]$$

In this equation, the constant term and the $1/\lambda^4$ term are due to the integration of the Poynting vector over the scattering volume. The average refractive index, n_0, the ensemble average of the index perturbations, $\langle\delta n^2\rangle$, and the correlation length, D, describe the statistical properties of the

scattering volume. The correlation length is cubed because of the statistical symmetry of the scattering volume in three dimensions. From a physical viewpoint, specific three-dimensional arrangements of the molecules repeat themselves throughout the media.

The Rayleigh attenuation for any optical media may be calculated if we can derive the $\langle \delta n^2 \rangle D^3$ term from its physical properties. For gases and pure liquids, the index perturbations are caused by the Brownian motion of the molecules, and the Rayleigh attenuation coefficient has been calculated from classical electromagnetics and thermodynamics to be

$$\langle \delta n^2 \rangle D^3 = \frac{1}{4} n_0^8 p^2 B_T (K_B T), \qquad [3.3]$$

where p is the photoelastic coefficient, B_T is the isothermal compressibility, K_B is the Boltzman constant, and T is the absolute temperature. The $K_B T$ product is the thermodynamic driving energy for the molecular density fluctuations, and the $n_0^8 p^2$ factor determines the conversion of the density fluctuations into refractive index perturbations [12,20,21].

The photoelastic coefficient p describes the strain-induced change in the refractive index in the axis of propagation. A strain of ε produces a change in the refractive index given by the relationship[22]

$$\delta n_z = -\frac{n_0^3}{2} p \, \varepsilon . \qquad [3.4]$$

B_T, the isothermal compressibility, is a measure of the compliancy of the medium to the driving energy. Values are tabulated in handbooks according to the following formula[23]

$$B_T = -\frac{1}{V}\left[\frac{dV}{dP}\right]_T . \qquad [3.5]$$

For glassy materials, the random density fluctuations are not driven by the ambient temperature. Rather, they are frozen in during the solidification process. Cold glass still reflects the randomness prevailing at the molten state. The concept of the 'Fictive Temperature' was introduced to account for the frozen density fluctuations in glassy materials. The fictive temperature is close to the softening point of the glasses, and if heated to this temperature, the material would come into thermodynamic equilibrium[21].

The attenuation due to Rayleigh scattering for single component materials is calculated from Equations 3.2 and 3.3 to be[12,20,21]

$$\alpha_R = \frac{8\pi^3}{3\lambda^4} n_0^8 p^2 B_T K_B T \ . \qquad [3.6]$$

Multicomponent materials have some additional density fluctuations due to the different sizes of the constituent molecules. Polymers also have similar fluctuations due to the varying numbers of monomers in a chain. General expressions have been developed for materials with multiple components[17,21,24]. The net effect is an additional scattering term in Equation 3.6 for each constituent with the same λ^{-4} dependence. The magnitude of each term depends on the mean refractive index, molecular size and weight, and concentration level of the components.

3.2 CALCULATING THE RAYLEIGH COEFFICIENT

The Rayleigh attenuation coefficient may be calculated from Equation 3.2 if the correlation length, D, and the mean refractive index variation $\langle \delta n^2 \rangle$ are experimentally determined. For a sample slab of polymethyl methacrylate (PMMA), the correlation length was found to be 280 nm, and the mean squared refractive index variation was about 4×10^{-8} from the mean index of 1.49 for PMMA[25]. The attenuation is calculated to be 1.235 nepers/m or 5360 dB/km at 850 nm wavelength. This figure is on the order of 10^4 times higher than the attenuation in pure silica. The urea acrylate coatings used in optical fibres may have similar Rayleigh attenuation coefficients.

It is also possible to determine the Rayleigh attenuation coefficient from Equation 3.6 if all the material parameters are known[12]. From the physical parameters of fused silica presented in Table 3.1, α_R is calculated to be 0.35 nepers/km or 1.5 dB/km at 0.85 μm.

Table 3.1 Physical parameters for fused silica

Bulk Refractive Index	1.458
Fictive Temperature	1400°K
Isothermal Compressibility	6.8×10^{-12} cm^2/dyne
Photoelastic Coefficient	0.286

3.3 CALCULATING α_R FROM LOSS DATA

The general attenuation relationship presented in Equation [2.16] can be simplified by noting that $\alpha_A(\lambda)$, the absorption term, is negligible in modern glass fibres at a wavelength of 850 nm. Also neglecting the attenuation due to bending, and expressing the wavelength dependence of the attenuation due to Rayleigh scattering, we arrive at the relationship

$$\alpha_{total} = \alpha_R + \alpha_P = \frac{A_R}{\lambda 4} + \alpha_P , \qquad [3.7]$$

where A_R is a constant. If the total loss coefficient is known at two different frequencies, we may calculate α_R and α_P. The only limitation is that the chosen frequencies should be close together and not coincide with the absorption peaks present due to water and other impurities.

The Corguide® LDF™ CSB4 graded index multimode fibre with a 50/125 μm core and cladding diameter was one of the fibres used in the experiments. Total attenuation levels were available at 850 and 1300 nanometer wavelengths[26]. The available data are summarized in Table 3.2.

At a wavelength of 0.85 μm, α_R is calculated to be 2.165 dB/km. This value is larger than the 1.5 dB/km attenuation coefficient of pure silica calculated from Table 3.1 since this fibre has an added term to account for the concentration fluctuations of the doping material used to create the parabolic refractive index profile.

Table 3.2 Calculation of α_R from loss data

Wavelength (μm)	Total Loss	$\alpha_{total} = A_R/\lambda^4 + \alpha_P$
0.85 dB/km	2.42 dB/km	$\alpha_{total} = A_R/0.85^4 + \alpha_P$
1.30 dB/km	0.65 dB/km	$\alpha_{total} = A_R/1.3^4 + \alpha_P$
Coefficients	A_R= 1.13 (μm^4) dB/km	α_P= 0.254 dB/km
Rayleigh Attenuation Coefficient at λ = .85 μm		α_R= 2.165 dB/km

Chapter 4

THE BACKSCATTERED TRACE

Reflections occur at any breaks, splices, connectors and other physical faults in the fibre link where there is a discontinuity in the refractive index. If optical power is normally incident on an interface between two regions in the fibre with refractive indices n_b and n_a, then according to Fresnel's equations the fraction of power reflected will be

$$R_P = \left(\frac{n_a - n_b}{n_a + n_b}\right)^2 . \qquad [4.1]$$

For silica (n_a = 1.45, n_b = 1.00), a clean break will thus cause about 3.6% of the incident power to be reflected, and the reflected light level will be 14.4 dB below the incident power level. For much smaller discontinuities in the refractive index, such as at a splice or a connector, the reflection coefficient can be approximated by

$$R_P = \frac{1}{4}\left(\frac{\delta n}{n}\right)^2 . \qquad [4.2]$$

If the end of a silica fibre is immersed in a fluid whose refractive index is 2% different than silica, we would expect about 0.01% reflection from the end. Even with a good index matching liquid we will have a reflection level which is 40 dB below the incident power level. Such a small reflection is expressed as being '26 dB below the Fresnel reflection from a clean break.'

Rayleigh backscattering, smaller than this 0.01% reflection, is a challenge to the best detection methods, but since it is present along the whole length of the fibre, it is a superb diagnostic tool for optical fibre systems.

4.1 THEORY OF THE BACKSCATTERED TRACE

In this section, the total attenuation coefficient, and the Rayleigh attenuation coefficient, will be applied to light propagation in the optical fibre to derive the power received at the input end of the fibre due to Rayleigh scattering as a function of time. This function, called the backscattered trace, will be derived with the assumption that the total attenuation coefficient and the Rayleigh scattering coefficient are constant along the whole length of the fibre in the forward and backward directions. The calculations are simplified further by ignoring the variation of the Rayleigh coefficient due to the changing dopant concentration in the radial direction and the incident modal power distribution, and concentrating on the light scattered only once in the backward direction from small segments of the fibre as a monochromatic light pulse is propagating in the forward direction.

The input power is attenuated by a factor $a_f(z)$ after travelling a distance z through the fibre in the forward direction,

$$a_f(z) = e^{-\alpha_{Tz} z}, \qquad [4.3]$$

where α_{Tz} is the total attenuation coefficient per unit distance. At location z, this attenuated pulse suffers Rayleigh scattering in all directions. A small fraction, r_b, of this scattered light is captured in the numerical aperture of the fibre in the backward direction. Elaborate expressions exist for this term[15], but the simplified expression

$$r_b = \alpha_{Rz} \frac{(NA)^2}{4n_1^2}, \qquad [4.4]$$

where α_{Rz} is the Rayleigh attenuation coefficient per unit distance, is a good

approximation for a parabolic-profile multi-mode fibre with isotropic Rayleigh scattering[27,28]. The power that is captured in the backward direction will travel to the input end. If the same total loss coefficient is assumed in the backward direction, there is another attenuation factor,

$$a_b(z) = e^{-\alpha_{Tz} z}, \qquad [4.5]$$

for the return travel. So the total attenuation for the travel to and from location z is given by

$$a_r(z) = a_f(z) r_b a_b(z). \qquad [4.6]$$

This function, which describes the Rayleigh scattering behaviour of the fibre, can be used to calculate the power received at the input end of the fibre for arbitrary pulse shapes, and will be dubbed the 'Rayleigh attenuation function' of the fibre. Using Equations 4.3 to 4.6, the Rayleigh attenuation function is given by

$$a_r(z) = \alpha_{Rz} \frac{(NA)^2}{4n_1^2} e^{-2\,\alpha_{Tz} z}. \qquad [4.7]$$

The power received at the input end is usually expressed as a function of time elapsed since the launch of the input pulse. But the attenuation coefficients are usually given in nepers per unit distance. Observing that the elapsed time is for return travel to a location in the fibre, a distance to time transformation,

$$z = vt/2, \qquad [4.8]$$

needs to be used to transform $a_r(z)$ to a function of time,

$$a_r(t) = \alpha_{Rt} \frac{(NA)^2}{4n_1^2} e^{-2\,\alpha_{Tt} t}. \qquad [4.9]$$

The attenuation coefficients, expressed in nepers per unit time, are

$$\alpha_{Tt} = \alpha_{Tz} \frac{v}{2}, \qquad [4.10a]$$

and

$$\alpha_{Rt} = \alpha_{Rz} \frac{v}{2}. \qquad [4.10b]$$

The Rayleigh attenuation function can also be written as

$$a_r(t) = \alpha_{Rz} \frac{v(NA)^2}{8n_1^2} e^{-\alpha_{Tz} vt}. \qquad [4.11]$$

Since it is customary to express the attenuation coefficients in nepers per unit distance only, α_{Rz} and α_{Tz} will be replaced by α_R and α_T to conform with Chapters 2 and 3. The general form of the Rayleigh attenuation function will be accepted as

$$a_r(t) = \alpha_R \frac{v(NA)^2}{8n_1^2} e^{-\alpha_T vt}, \qquad [4.12]$$

where it is assumed that $a_r(t)$, α_R and α_T are all in units of nepers per unit distance.

For an arbitrary input pulse $P_i(t)$, the received backscatter trace would be the convolution of the backscatter impulse response and the pulse profile

$$B(t) = a_r(t) * P_i(t) = \int_{-\infty}^{+\infty} a_r(\xi) P_i(t-\xi) d\xi. \qquad [4.13]$$

For a rectangular pulse $P_i(t)$ of magnitude P_0 and width τ, the integral reduces to[19]

$$B(t) = \frac{P_0}{\alpha_T v} 2 \sinh\left(\alpha_T v \frac{\tau}{2} \right) a_r(t). \qquad [4.14]$$

The hyperbolic sine function may be replaced by its argument when the condition

$$\tau \ll \frac{2}{\alpha_T v} \qquad [4.15]$$

is satisfied. The backscatter trace for a short rectangular input pulse is thus

$$B(t) = (P_0\tau)\, a_r(t) = \frac{(P_0\tau) v \alpha_R (NA)^2}{8n_0^2}\, e^{-\alpha_T (vt)}, \qquad [4.16a]$$

which, when expressed as a function of z, takes the form

$$B(z) = (P_0\tau)\, a_r(z) = \frac{(P_0\tau)\, v \alpha_R (NA)^2}{8n_0^2}\, e^{-2\alpha_T z}. \qquad [4.16b]$$

A 'Reflection Coefficient', $\boldsymbol{R}$, may be defined as the ratio of the received backscattered power to the forward propagating power[29].

$$\boldsymbol{R}(z) = -10 \log_{10}\left[\frac{B(z)}{P_f(z)}\right] \qquad [4.17]$$

The forward power at location z is given by

$$P_f(z) = P_0 e^{-\alpha_T z}. \qquad [4.18]$$

Substituting the expression for B(z) from [4.16b] and $P_f(z)$ from [4.18] into [4.17] and rearranging the terms, we obtain a simplified expression for the Reflection Coefficient at location z of the fibre to be

$$\boldsymbol{R}(z) = 10 \log_{10}\left[\frac{B(z/2)}{P_0}\right] \text{dB}. \qquad [4.19]$$

4.2 CALCULATED TRACE FOR THE TEST FIBRE

The Rayleigh attenuation coeficient was calculated in Chapter 3 from the manufacturer's specifications. The relevent parameters of the test fibre are repeated in Table 4.1 so that the backscatter trace may be calculated.

Table 4.1 Backscatter parameters of a test fibre

n_0=1.4655	NA = 0.2
v=c/n=2.047 × 10^8 m/s	$\Delta z/\Delta t$ = 1.023 × 10^8 m/s ≈ 10 cm/ns
α_R=2.16 dB/km = 0.497 nepers/km	α_T =2.414 dB/km = 0.555 nepers/km

The condition set forth in Equation 4.15 is satisfied for pulses shorter than 1.8 nanoseconds. For a launched rectangular pulse of peak power 10 mW, and width 100 ps, the pulse energy ($P_0\tau$) is 1 picoJoule. The backscattered trace as a function of z, calculated from Equation 4.16b, is

$$B(z) = 0.24\, e^{-1.11\times10^{-3} z} \text{ (nanowatts)} . \qquad [4.21]$$

The backscatter trace from Equation 4.21 is plotted for three different intervals in Figure 4.1. The exponential nature of the trace is apparent when the received power is plotted from 0 to 5000 metres. For small segments of the fibre the backscatter trace resembles a straight line. The trace is essentially a constant line at 0.22 nW for the 1 metre segment between 70 and 71 metres.

Since the energy of an individual photon is 2.34 × 10^{-19} Joules at a wavelength of 0.85 μm from Planck's relationship, the received power level corresponds to a photon arrival rate of 0.94 × 10^9 photons per second. The backscattering process will therefore deliver approximately 1 photon every nanosecond to the detector end of the fibre when a 100 ps wide rectangular pulse with a 10 mW power level is launched into the input end of the fibre.

The 'Reflection Coefficient', R, determined from Equation 4.19 using the same pulse width, is

$$R(z) = (-76 - 2.44\times10^{-3}\, z)\ \text{dB} . \qquad [4.22]$$

This relationship illustrates the very low levels of return signals encountered in Rayleigh backscattering experiments. Immediately after launch, we encounter power levels 76 dB below input levels.

4.3 BACKSCATTERING FROM PERTURBED FIBRES

The backscattered traces presented in Figure 4.1 represent only a homogeneous fibre with no additional perturbations. The statistical parameter fluctuations that result in mode coupling and radiation loss in the forward propagating modes, have effects which are similar in nature but different in magnitude on the backward propagating modes. The cause of this discrepancy is the different modal power distributions in the forward and backward directions. The Rayleigh scattering coefficient described in Chapter 3 is not a constant but a function of the refractive index profile and the modal power distribution[15]. Statistical parameter fluctuations result in granularity in the backscattered trace. These random perturbations will be neglected for simplicity and only the effect of applied bends and microbends will be considered.

A perturbation function may be defined as an additional modulating effect on the power at a location of the fibre, independent of the Rayleigh attenuation function. For a bend or a microbend, this function will be zero before, and a downward step after, the perturbation region. The magnitude of the step will be the total attenuation or 'insertion loss' of the bend region.

Within the region, the perturbation function will depend on the geometry of the bend or microbend, and the power distribution existing in the core, cladding, and beyond. Usually, there will be a downward slope connecting values of the perturbation function at the beginning and end of the bend region. However, under appropriate conditions, it is possible to have narrow peaks for the function in this region that will appear as enhancements of the backscatter trace at the input end.

If a perturbation function $\mathbf{d}(z)$ is present in the fibre, the total effect on the backscatter trace would be given by[28]

$$B(z) = \int_{-\infty}^{+\infty} \left\{ a_r(\xi) + \mathbf{d}(\xi) \right\} P_i(z-\xi) d\xi \,, \qquad [4.24]$$

where $P_i(z)$ is the input pulse. The result will be a linear superposition of the Rayleigh backscatter trace B(z) and the perturbation trace

$$D(z) = \int_{-\infty}^{+\infty} D(\xi) P_i(z-\xi) d\xi. \qquad [4.25]$$

The shape of D(z) cannot be determined without knowing the shape of the perturbation function, but some generalizations may be made for special cases. D(z) will mimic the perturbation function for narrow input pulses, while a large input pulse will produce a trace that reflects the input pulse shape. In all cases, the width of D(z) will be the sum of the width of the pulse and d(z) due to the convolution.

For narrow rectangular input pulses, the perturbation trace may be approximated by the product of the pulse height and the area under the perturbation function in a window equal to the width of the pulse.

4.4 BACKSCATTERED TRACE FROM BENDS

The attenuation produced by transmission through a bend region should be reflected in the backscatter trace. Since the modal power distributions are different in the forward and backward propagating modes[15], the attenuation levels calculated in Chapter 2 do not give accurate results when applied to the backscattered light. A larger percentage of power resides in the higher order modes for backscattered light[3] resulting in higher attenuation by the same bend for the backscattered light.

A theoretical study has been performed to determine the nature of the backscatter trace from fibre bends as a function of the bend radius and length and its dependence on pulse width and modal power distribution[30]. It was found that the loss is very sensitive to the MPD and the curvature spectrum. The trace will show a single drop when the spatial pulse width is much larger than the bend region; otherwise separate features may appear as the pulse transits the front and rear of the bend.

When the transition region between the straight fibre and the bend is of the order of the width of the waveguide, a 'reflection peak' is calculated to appear if the spatial pulse width is smaller than the bent region. The additional scattering produced by the shift in the modal power distribution within the bent region and captured into the backward propagating bound modes is speculated to be the cause of the reflection peak.

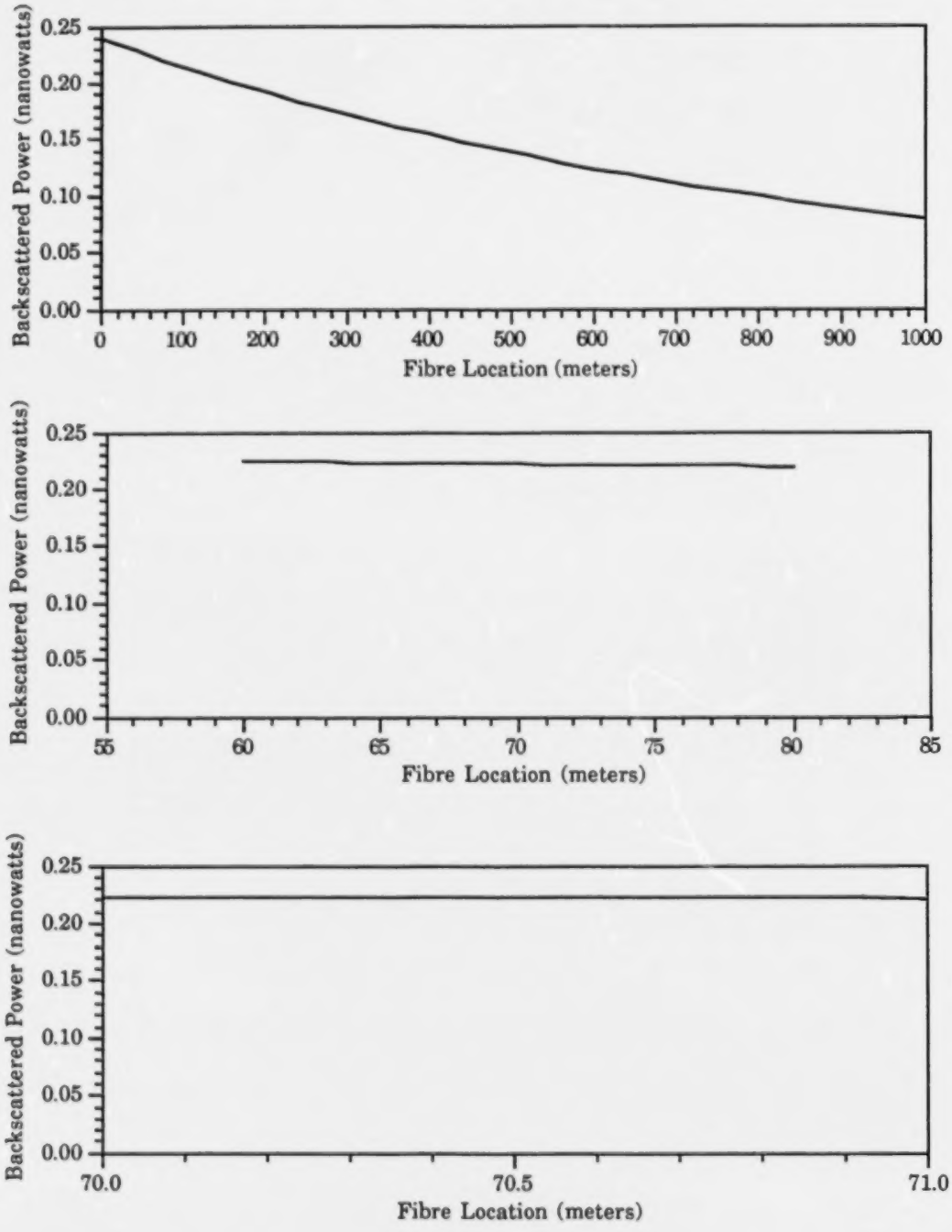

Figure 4.1 The backscatter trace for a short 1 picoJoule pulse from three different intervals.

Chapter 5

OPTICAL TIME DOMAIN REFLECTOMETRY

Optical Time Domain Reflectometry (OTDR) is a technique for non-destructive single-ended measurements on an optical fibre. It is analogous to Radio Detection and Ranging (RADAR) in the optical domain. Light pulses are sent down the experimental fibre and the reflected light intensity is plotted against the time delay.

5.1 DESIGNING AN OTDR

A typical OTDR setup is shown in Figure 5.1. A switchable light source launches a pulse into an optical fibre through a coupler which also directs the returning signal to an optical detection mechanism. The detected signal is then suitably processed for display or analysis.

The light source is chosen to be a laser capable of producing short pulses with high peak power. The first OTDRs used GaAs injection lasers which produced 5 to 150 ns pulses at the 850 nm wavelength region. The PPL30K optical source module used in our experiments uses a GaAs/GaAlAs semiconductor laser diode with greater than 150 mW peak power, less than 75 ps pulse FWHM, and a maximum repetition rate of 30,000 pulses per second[31]. For longer wavelengths, semiconductor laser diodes with similar specifications are not available yet, and Q-switched Nd:Yag lasers (at 1300 nm) and Erbium Glass lasers (at 1550 nm) have been used in experimental OTDRs[32].

The directional coupler performs two separate functions. It allows efficient coupling of the laser pulse into the fibre with low loss levels. It also directs the reflected and backscattered light to the optical detector. A fused bi-conical taper coupler[32] and beam splitter[27] were among the earliest types of directional couplers used. Fused fibre couplers[31] and their integrated optics counterparts are most commonly used in commercial OTDRs. Other types of couplers used in experimental OTDRs include a Polarizing Prism Beam Splitter and an Acoustooptical Deflector.

The selection of an optical detection system to be used in an OTDR setup is dictated by the required minimum detectable power, signal-to-noise ratio, range loss budget, and distance resolution. Although photomultiplier tubes have been used in early OTDRs[27], recent instruments operating at 850 nm wavelengths use silicon avalanche photodiodes (APDs) as a sensitive and low noise detector[32].

The Fresnel reflection at the input end of the fibre, which is several orders of magnitude higher than the backscattered light, will saturate the detector for some amount of time and contribute to a long 'dead zone', or a certain length of the fibre where backscatter measurement is not possible. All practical OTDRs include mechanisms to either reduce the reflection or to shield the detector from it for a short time. Electronic gating or delayed activation is possible for photomultipliers[27] and avalanche photodiodes. For other types of detectors, shielding may be achieved by using an acoustooptic deflector just to deflect the light from the input end[32]. Passive methods used to reduce the reflection include the use of index matching liquids, cross polarizers, and tapered couplers.

5.2 SENSITIVITY AND RESOLUTION

The backscattered trace was calculated in Chapter 4 without consideration for the attenuation of the input laser pulse and the backscattered light by the directional coupler and the splices and connectors in the OTDR system. The signal level arriving at the detector from a location z along the fibre is given by the range Equation of an OTDR

$$P_D = P_I - P_R - (\boldsymbol{R} + C) \text{ dBm} \qquad [5.1]$$

where P_I is the peak laser power in dBm, P_R is the total attenuation for the signal for the travel to and from z, $\boldsymbol{R}$ is the Reflection Coefficient at z , and C is the total length independent loss in the path of the light to and from location z. $\boldsymbol{R}$ is defined by Equation 4.19 for backscattering, and by Equation 4.2 converted to dB for splices and connectors.

The value of C for the Opto-Electronics OTDR is given as 26 dB to the bulkhead. The laser module produces 150 mW or 22 dBm peak power, and the reflection coefficient at 100 metres is calculated to be –76.24 dB from Equation 4.22. The two-way propagation loss for this distance is 0.48 dB. The backscattered light level from 100 metres is calculated to be –80.72 dBm or 8.5×10^{-12} Watts.

The minimum power level that can be detected by a detector system of bandwidth BW and noise equivalent power of NEP is given by the relationship

$$P_{min} = (NEP)\sqrt{BW} \qquad [5.2]$$

The noise equivalent power for a detector system is defined as the power level per unit bandwidth for a signal to noise ratio of unity.

The bandwidth is usually determined by the Nyquist criterion from the pulse width,

$$BW = 1/(2\tau)\,. \qquad [5.3]$$

A typical analogue detection system consists of a silicon avalanche photodiode and a low noise amplifier. The NEP of such a system is approximately 10^{-12} W/$\sqrt{\text{Hz}}$ at room temperature[10], and the detection bandwidth required for a 100 ps pulse is 5×10^{9} Hz. The minimum detectable power for direct detection by this system will be 70 nanowatts or –42 dBm. So direct detection is impossible without modification of the system.

Increasing the pulsewidth is the easiest improvement to achieve, but this comes at a sacrifice of the spatial resolution. The minimum detectable spatial separation for a pulse of width τ is

$$\delta z_{min} = v\,\tau / 2\,, \qquad [5.4]$$

where v is the group velocity. The detector and amplifier may also be cooled to reduce the NEP, but this leads to bulkier systems. The most commonly used method for improving the performance of receiver systems is to use signal averaging. If the results of N independent measurements are averaged, the SNR improves by a factor of N and consequently, the minimum detectable power is reduced[29] by a factor of $\sqrt{N}$. The analogue circuitry is subject to drift for long averaging times.

Another method of improving the signal to noise ratio is to detect the backscatter levels through digital photon counting. In the photon counting method, the silicon APD is biased slightly above its breakdown voltage. As a result, a single photon may initiate an avalanche. This method, defined as the Geiger mode, is simple to implement as it requires no sophisticated

amplifiers and the signal averaging and processing may be carried out digitally. The NEP of the detector has been improved to 10^{-16} watts/$\sqrt{Hz}$ before averaging at room temperature. The photon counting method is ideal for the detection of the backscatter trace over long ranges, but since it requires the arrival of no more than a single photon during a measurement interval, and the system is not suited for measuring large reflections.

5.3 A PHOTON COUNTING OTDR

The parameters of a photon counting OTDR system are the time delay T_0, the time division D, and the number of measurements N. The length of the fibre being observed is divided into an arbitrary M steps. The return time of flight from each of these M locations is determined by the relationship

$$T_i = T_0 + i\,D\ ;\ (i = 0 \text{ to } M\text{-}1). \qquad [5.5]$$

For each of these M steps, the time delay generator triggers the laser and waits precisely for the time interval T_i to elapse before initiating the operation of the APD. The photon counter stays on for a period T_{on} and if an avalanche is created, the resulting output current pulse is compared by the pulse height discriminator to determine whether the pulse was initiated by dark current or by the actual arrival of a photon. The output of this discriminator is either 0 or 1. If the output is 1, the i^{th} counter of the photon count array is incremented by 1. The process is repeated N times for each T_i. If the laser repetition rate is R Hz, then the whole process takes approximately

$$T_{total} = (N \times M) / R \text{ seconds} \qquad [5.6]$$

The incrementation process for each count must be performed in less than

1/R seconds. The lowest repetition rate is controlled by the drift in the analog circuitry that provides the bias voltage to the APD and the discriminator voltage. The highest repetition rate achievable is limited by the range requirement. If the fibre end is L metres away, then R should be no higher than

$$R_{max} = v / 2L \qquad [5.7]$$

to avoid receiving backscattered light pulses from two different locations of the fibre at the same time.

For M = 256 steps, and R = 30 Khz, if 2^{16} or 65536 samples were to be taken, the total elapsed time would be approximately 10 minutes. This is almost the limit for acceptable drift for the bias circuitry.

5.4 OPERATION OF THE DETECTOR

The avalanche photodiode is operated in Geiger mode for photon counting operations in an OTDR. In this mode, the APD is biased well above its breakdown voltage so that once an avalanche is inititated, the photocurrent is multiplied until limited by the diode resistance, or by the impedance of the diode circuit[33].

The probability of an avalanche breakdown occuring when a certain number of photons arrives at the APD in an interval is determined by complex functions of the geometry of the diode structure and the bias voltage[34,35]. The simplified relationship

$$p_{bkdn}(\text{n photons}) = 1 - \exp[-n\eta] \qquad [5.8]$$

approximates the probability of an avalanche breakdown occuring when

exactly n photons arrive at the APD during an interval[16]. The parameter η describes the photon counting quantum efficiency of the APD.

If the APD is operating in Geiger mode in the interval T_{on}, the mean number of photons arriving at that interval will be

$$m = (P_{avg} T_{on}) / (h\nu) \qquad [5.9]$$

where P_{avg} is the average power being received, and $(h\nu)$ is the energy of a single photon from Planck's relationship. The probability of exactly n photons impinging on the APD in the interval T_{on} for this mean number of photons is given by the Poisson distribution

$$p(n) = \frac{m^n}{n!} \exp [- m] . \qquad [5.10]$$

This function is plotted in Figure 5.2 for the probability of no photon, one photon, or more than one photon arriving at the interval.

The probability of an avalanche breakdown occuring for a mean level of m photons may be determined from Equations 5.8 and 5.10 as

$$p_{bkdn}\Big|_m = \sum_{n=0}^{\infty} \frac{m^n}{n!} e^{-m} [1 - e^{-n\eta}] , \qquad [5.11]$$

which reduces to

$$p_{bkdn}\Big|_m = 1 - \exp [- m(1 - e^{-\eta})] . \qquad [5.12]$$

This probability is plotted for three values of η in Figure 5.3. It is shown that even for $\eta = 1$, the probability of avalanche breakdown does not reach 1 until an average of 10 photons are arriving at the APD in the interval.

When an APD is excessively reversed biased, the quantum efficiency may reach 0.1 at the expense of high dark current rate. The probability function is plotted again for $\eta = 0.1$ in Figure 5.4 to show the linearity of the

function for the mean arrival rate of less than one photon in the interval. The slope of the function can be approximated by η for $m < 1$.

If there are C_i counts accumulated in the i^{th} counter after a total of N pulses have been sent, then the ratio (C_i/N) represents the probability of a photon count being recorded from the location corresponding to T_i. This ratio, defined as the 'Photon Detection Ratio' or PDR, is the only measure of the power level from that location of the fibre that is detected by the photon counting OTDR.

Using the PDR as the probability of an avalanche breakdown in Equation 5.12, the quantity m, or the average number of photons arriving from location T_i, may be calculated. The average power level corresponding to m can be calculated from Equation 5.9 to be

$$P_{avg} = \frac{-\ln(1-PDR)}{1-e^{-\eta}} \frac{h\nu}{T_{on}} \quad . \qquad [5.13]$$

When η is much smaller than 1, which is true for current photon counting OTDRs, Equation 5.13 may be simplified as

$$P_{avg} = \frac{-\ln(1-PDR)}{\eta} \frac{h\nu}{T_{on}} \quad . \qquad [5.14]$$

From this relationship, it is seen that the 'Photon Detection Ratio' is a non-linear representation of the backscattered power level. When the PDR is kept below 0.2, a linear relationship between the PDR and the backscattered power can be assumed.

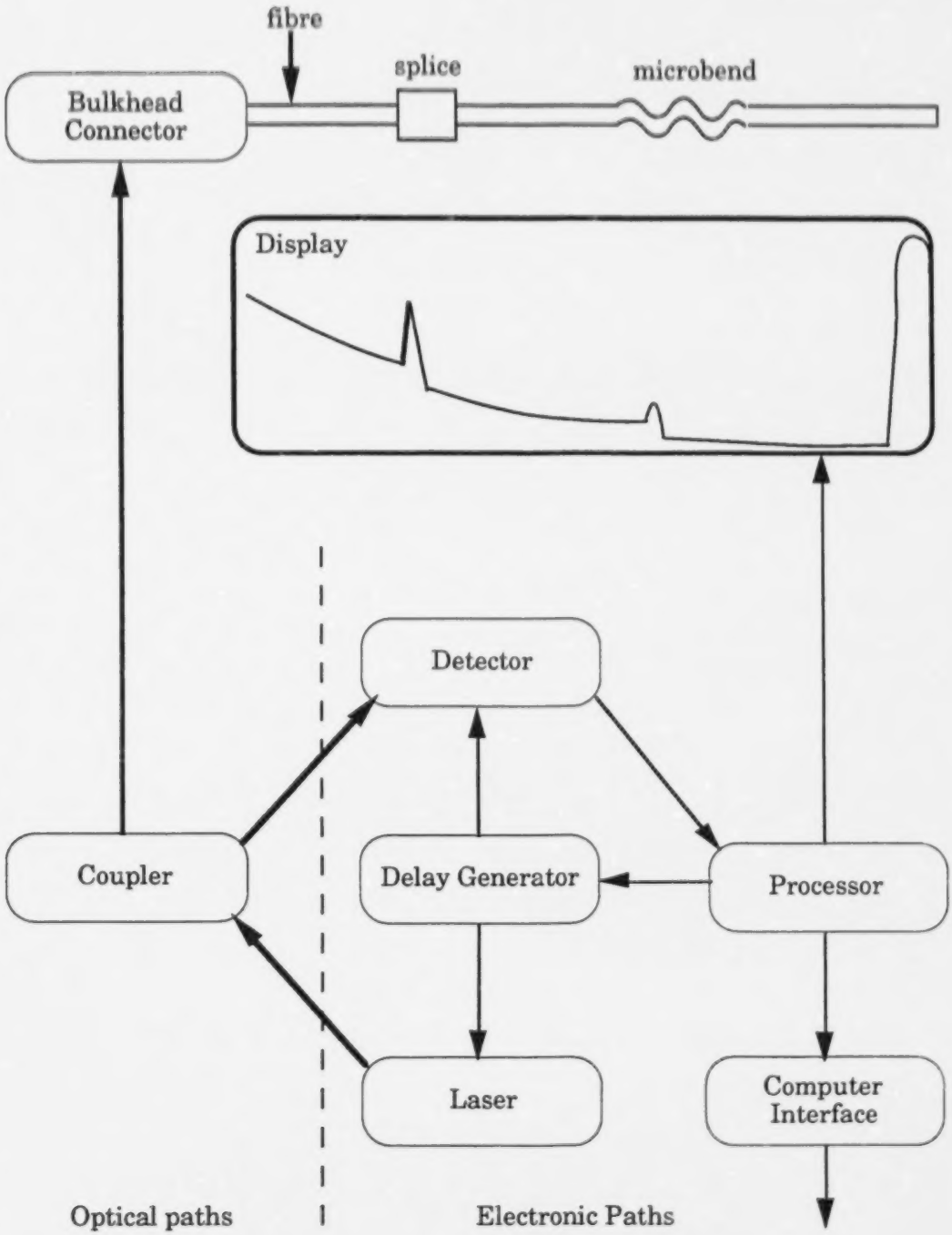

Figure 5.1 The Optical Time Domain Reflectometer

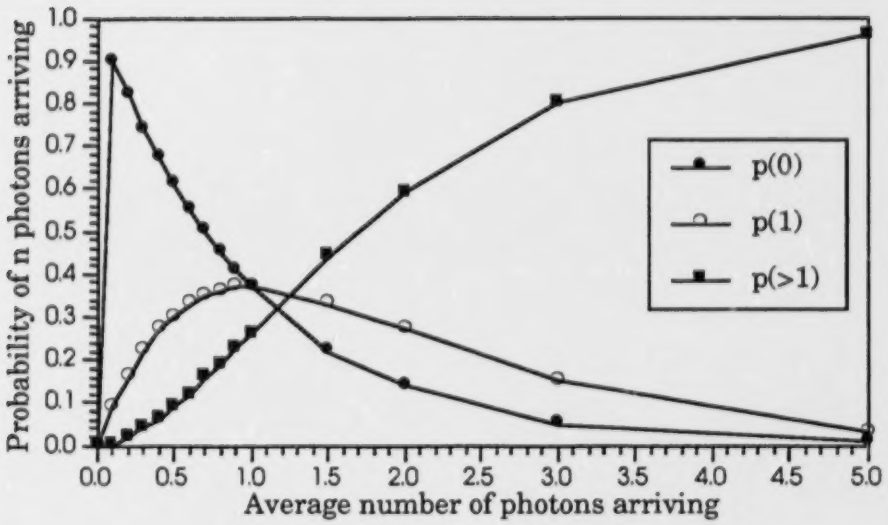

Figure 5.2 The probability of exactly none, one, or more than one photons arriving at the detector for a given average level of arriving photons.

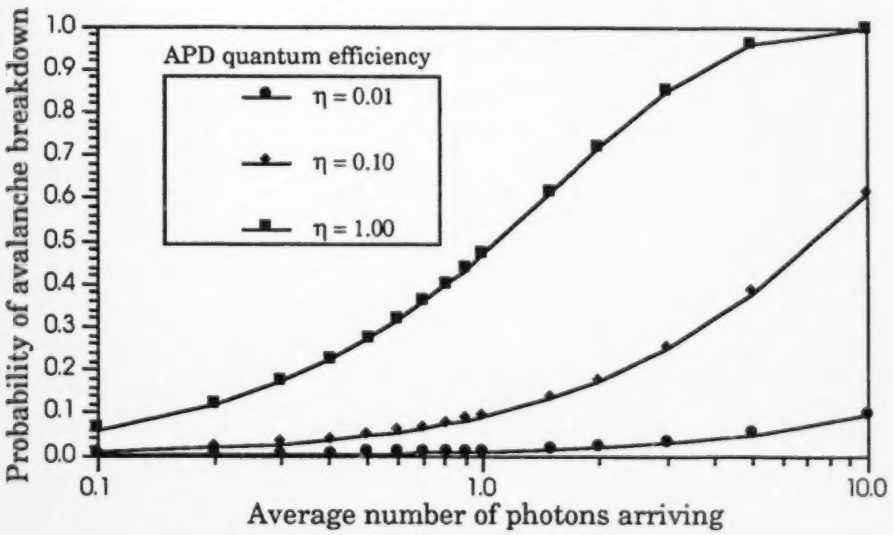

Figure 5.3 The Probability of an avalanche breakdown when an average of n photons are arriving at the APD.

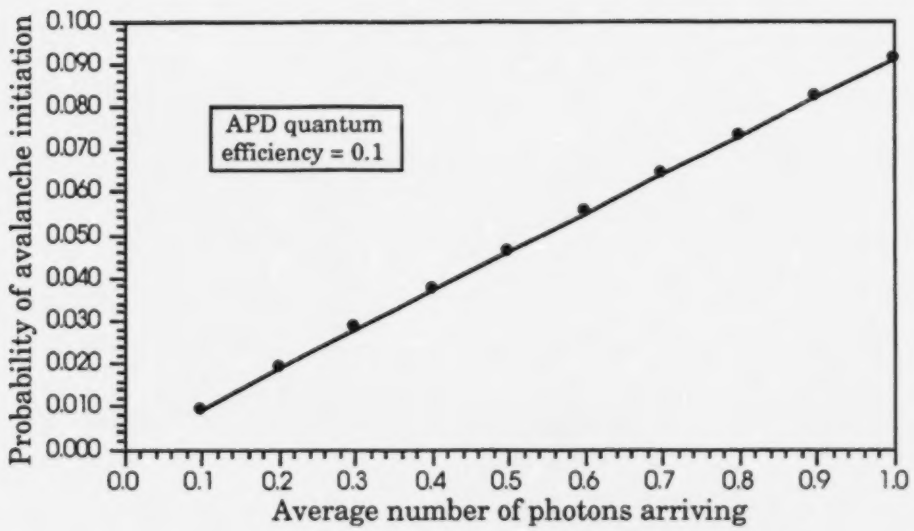

Figure 5.4 The linearity of the probability function of avalanche breakdown for less than one photon per interval.

Chapter 6

THE EXPERIMENTS

A general bender instrument, shown in Figure 6.1, was designed and built to enable different types of bends to be produced. The model 416 precision vertical translation stage from Newport Corp. allowed bend amplitudes from 1 μm to 13 mm with an accuracy of 1 μm per 1 mm of travel. The maximum load applied to the bend could be 15 Kg. A series 200 load cell from PCB Piezotronics was used to determine the force being applied and an x-y plotter was used to record it. Sets of plates were designed to allow periodic microbends by means of V-grooves or thin wires. The fibre was held in place by two poles resting on a ring that could be rotated and translated.

The TDR20 Millimeter Resolution OTDR System[37] and the MF20 Pico-second Fibre Optic System (PFOS)[31], both manufactured by Opto-Electronics Inc., and a FOT92 optical power meter were used during the experiments. The PFOS was equipped with a PPL30K diode laser operating at 850 nm and producing 150 mW of peak power in 100 ps pulses. The photodetector was the PPC10 photon counting module. The silicon APD in the module is biased above its breakdown voltage to operate in the 'Geiger' mode. The detector window setting of 0.5 ns was used throughout the experiments, resulting in a dark count rate of less than 0.04 per second. The PDG20 delay generator provided the laser module with a 30 KHz trigger rate. It also turned on the photon counting mode of the APD after a variable delay. The timing jitter of the delay module is less than 5 ps.

As explained in Chapter 5, three settings were necessary for each OTDR data acquisition set-up: T_0, the delay , D, the time division, and N, the number of measurements to be averaged. These numbers could be entered manually, and the backscatter trace could be output to an oscilloscope. However, custom software was developed to facilitate data acquisition.

6.1 SOFTWARE DESIGN

The 'Senlab' data acquisition software was designed to provide easy access to the OTDR. Core subroutines were developed and tested for communicating with the OTDR through a GPIB (IEEE-488) bus, and with the power meter through the serial (RS-232) port. The signal made available to the oscilloscope display was scaled by the OTDR processor with consideration for that display only, and was not found suitable for determining the photon counts. The actual photon count was extracted from the OTDR as a 24 bit integer.

A user interface was added to allow interactive or automated data acquisition, conversion and display. The display routine allowed superimposition of 14 previous measurements. The data could be saved automatically in files with unique names and an entry made in a log file with all the OTDR settings employed and optional comments entered during the measurements. The power meter data was also saved with the same filename, but with a different extension. The software was designed so that unattended operation would be possible with different OTDR settings stored in a file. For interactive sessions, the last settings used were

remembered. The 'Senlab' software was found to be very useful for the initial visualization of the backscatter trace and taking rapid measurements. More than 30 interactive or 60 automated data acquisition runs per hour were made possible by the software. A flow diagram of 'Senlab' is presented in Figure 6.2.

6.2 THE EFFECTS STUDIED

One of the objectives of the experiments was to investigate the peaks of enhanced backscattering at bend locations that have been previously observed, but not studied in detail[3,10]. Several microbending experiments were carried out in an effort to reproduce, and study in detail, the backscattering enhancement.

A specially constructed fibre sensor, manufactured by Herga Corporation[38], was studied in one experiment. It was found unsuitable for enhanced backscattering since the distortion amplitude required to produce measurable peaks caused permanent damage of the fibre jacket by the thin polymer strands wrapped around the fibre.

In another experiment, periodic microbending of the fibre by parallel, thin metal wires was found to produce enhanced backscattering when the distortion amplitude was much larger than the core diameter of the fibre. The arrangement of the bender for these experiments is presented in Figure 6.3. After repeated measurements at the same location, some permanent and visible damage to the fibre jacket was observed.

In a series of experiments, single bends of the fibre pressed against an elastic foundation were studied in detail. Arrangement of the bender instrument for these measurements is presented in Figure 6.4. The thin mylar that was glued one side of the foam did not allow sufficient backscattering enhancement, so different types of surfaces were experimented with. Placing the fibre on a plain note paper with adhesive on one side, and a paper tape with adhesive on both sides were compared.

The effect of pressing the fibre with metal rods of different diameters was investigated. Two different rod diameters, 1.55 mm and 2.35 mm, were used on the two different surfaces to produce a wide variety of bend shapes and compare the resulting losses and backscattering enhancement.

The effect of the fibre jacket on the peak levels was investigated by stripping the jacket material at the bend location using a solvent. Enamel paint was sprayed on the bare fibre to observe if there were changes to the backscattered light level.

During these measurements, a video image capture system was used to record the profile of the bent fibre. Since the maximum amplitude of the bent fibre was less than 2.5 mm, the closeness of the parallel plates of the bender platform caused difficulties in obtaining enough lighting and magnification. However, images were captured using a high power xenon lamp focused onto the bend region using a flat optical ribbon. The details and results of the experiments are provided in the next chapter. Some photographs of the bent fibre profiles are also presented.

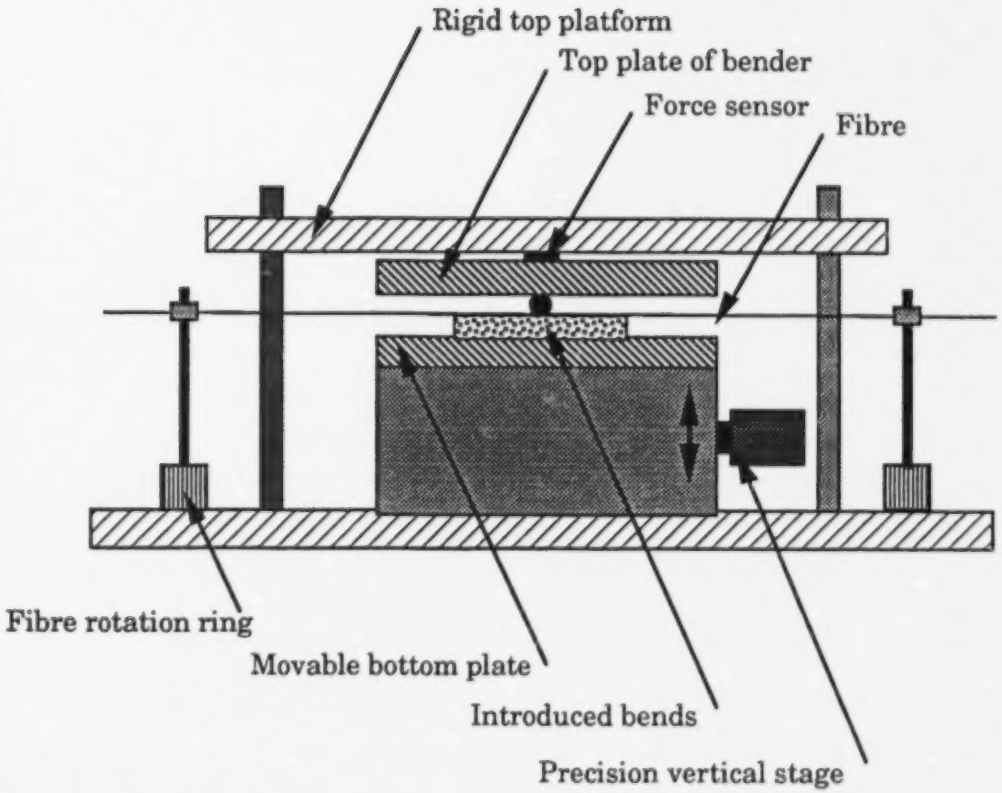

Figure 6.1 The bender instrument

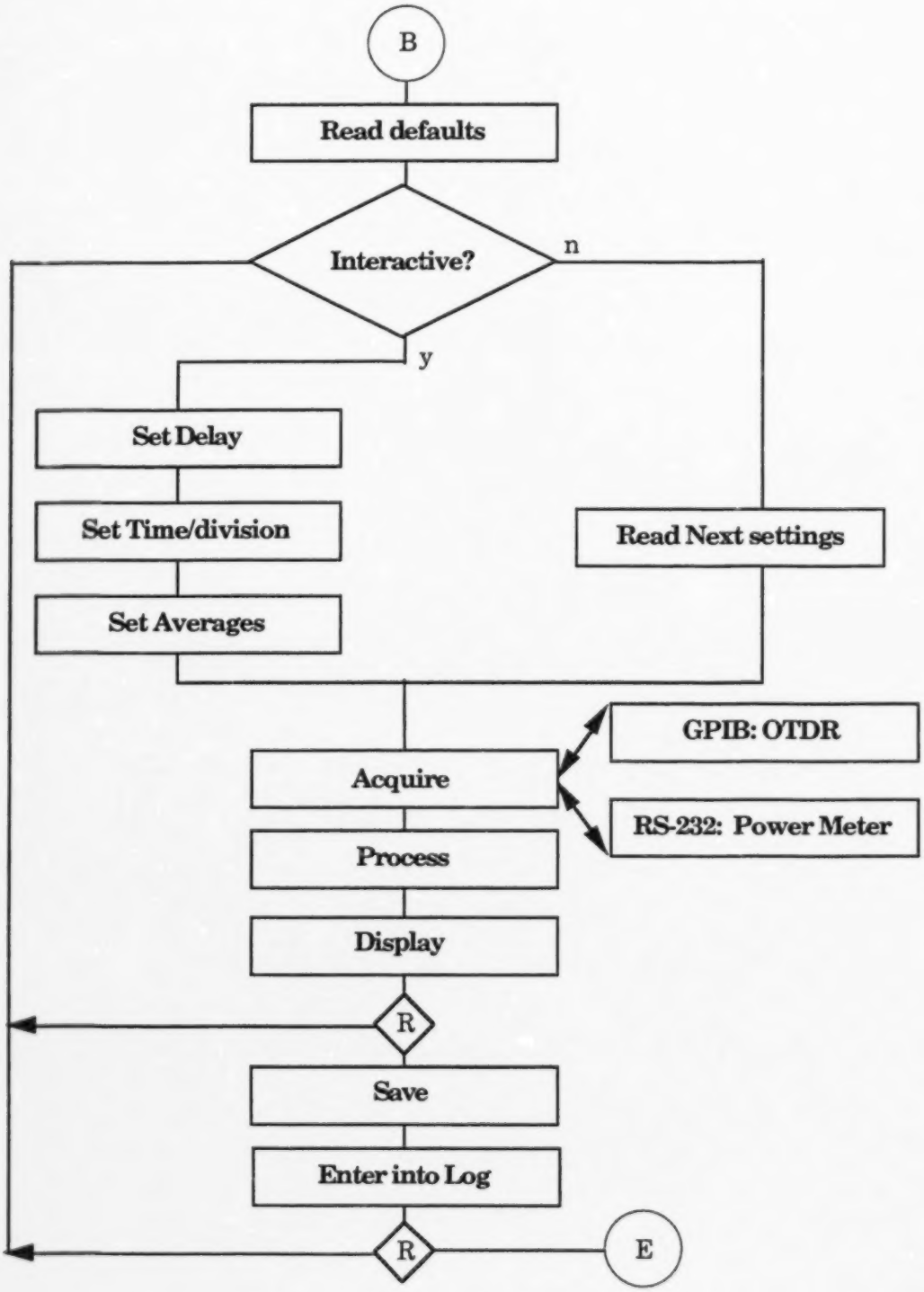

Figure 6.2 Flow diagram of the 'SenLab' software

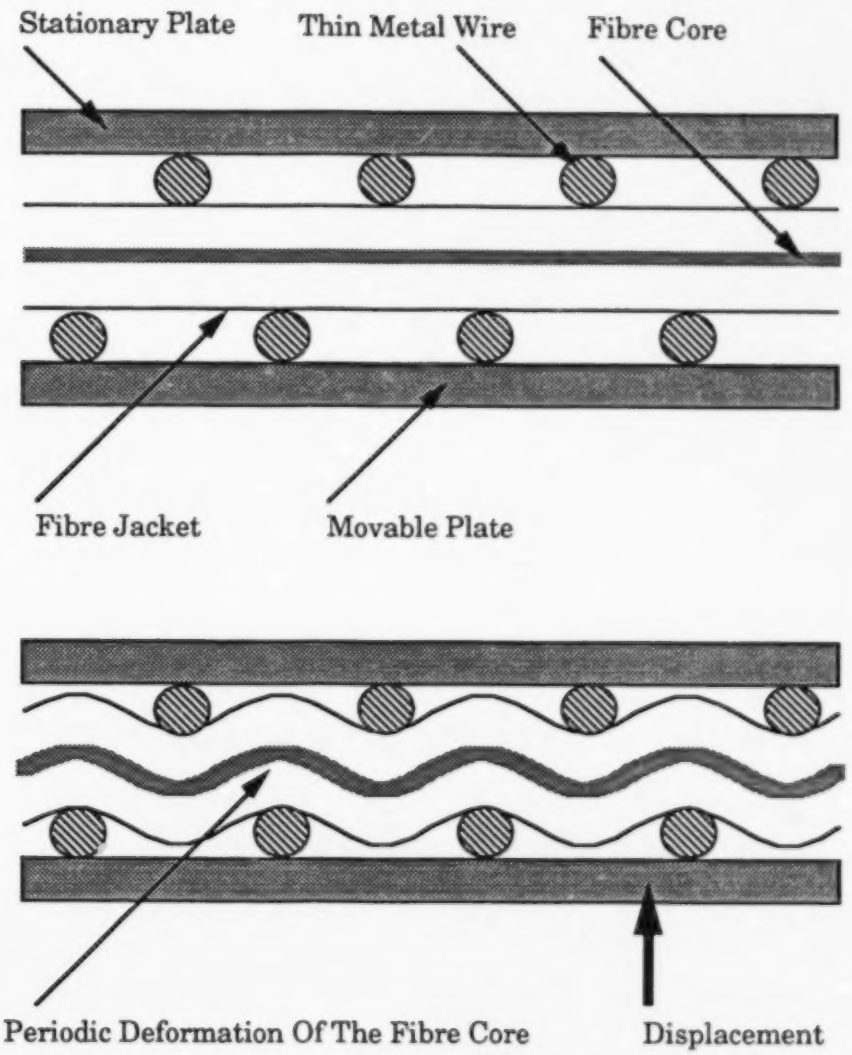

Figure 6.3 Setup for periodic bending experiments

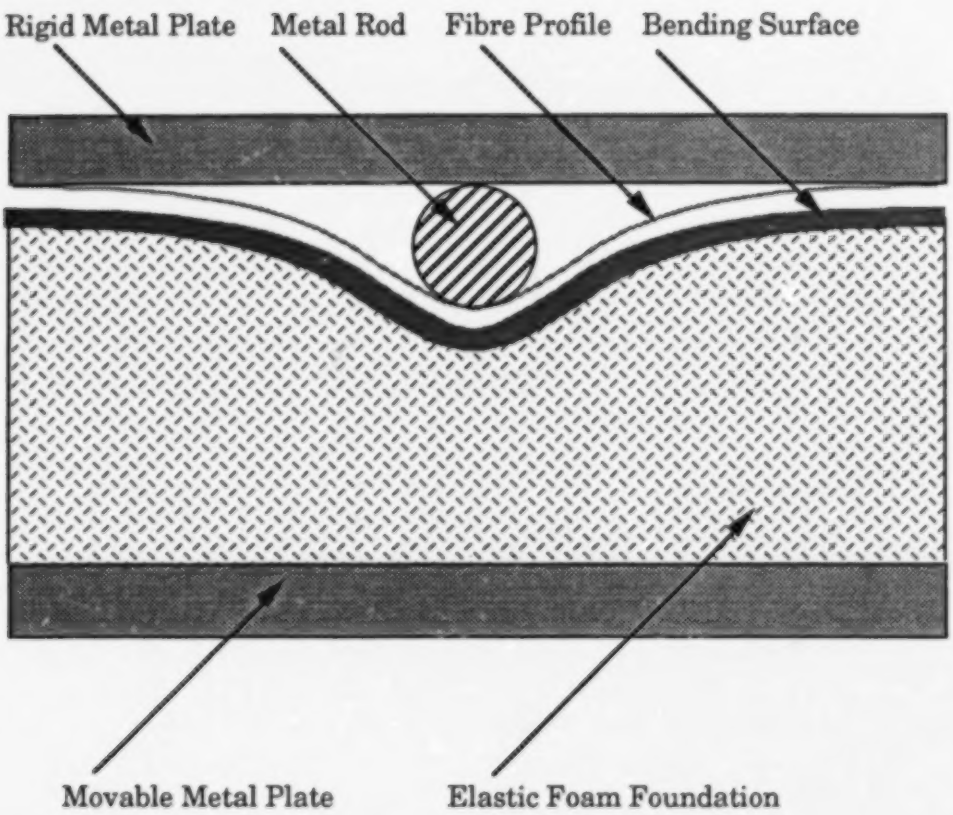

Figure 6.4 Setup for single bend experiments

Chapter 7

ANALYSIS OF RESULTS

Data analysis software were written to extract information from the OTDR and Power Meter data files, and to visualize the relationship between various data sets. A flow diagram for the software is presented in Figure 7.1. The baseline of a given data set was determined from a combination of an OTDR data file with minimum loss and a power meter file with the highest power level at the end of the fibre. When this approach was not applicable, a value for the base power level was typed in. The OTDR data was normalized by dividing the received photon count by the number of laser pulses sent. This 'Photon Detection Ratio', or PDR, was used throughout the analysis, and represents the probability that a photon count will be recorded from a location for a given laser pulse. If the quantum efficiency of photon counting of the APD used in the OTDR was known, this value could be converted to actual power levels by using the relationship in Equation 5.13.

An OTDR data file contains 256 points, each indicating the photon count received from a 0.5 ns interval starting at a delayed time T_i given by the relationship in Equation 5.5. The time axis was converted to distances along the fibre using the relationship $z = vt/2$. The initial level of each OTDR data file was determined from 20 to 30 data points located before the peak, if present, and the final level was determined from 20 to 30 points after the peak. Three standard deviations of each of these selected points were taken as the error for that measurement.

The peak level was determined by parabolic curve fitting of 5 to 13 points around the maximum, if the maximum exceeded three standard deviations from the base level. The errors of the peak were determined from the relationship,

$$\text{Error(Peak)} = 1 - \text{Error(Initial)} \times \sqrt{\frac{\text{Peak level}}{\text{Initial level}}} \,. \qquad [7.1]$$

These values of the errors are conservative estimates. When repeated measurements were taken under the same conditions, the peak level fluctuations were found to be 2 to 6 times smaller than these values.

The loss of the backscattered trace was determined from the relationship,

$$\text{OTDR Loss} = 1 - \sqrt{\frac{\text{final trace level}}{\text{initial trace level}}} \,. \qquad [7.2]$$

The square root is necessary because of the two-way path of the light through the lossy region. The power meter loss level was calculated as the ratio of the power meter reading and the base power level.

The method of propagation of errors was used as required to calculate the error bars for all plots presented in this chapter. The random fluctuations of the initial levels of the OTDR traces contributed to large error bars on some occasions.

7.1 PERIODIC MICROBENDS

The raw data from a few of the microbend experiments is presented in Figure 7.2 to help visualize the backscattered traces from periodic microbends of various amplitudes. The peak and loss levels are plotted in Figures 7.3 and 7.4. The loss determined from the OTDR trace is higher than that from the power meter because of the difference in the modal power distribution in the forward and backward directions.

A qualitative comparison may be made between the results of this experiment and a similar one mentioned in the literature[3]. The fibre parameters were roughly similar, but in plots provided in Reference 3, the level of the peak at the microbend location was just barely visible when the loss was 6 dB. We have succeeded in producing a visible and measurable peak which is 3 dB above the backscatter level before the microbend region (the trace for 210 μm in Figure 7.2), when the loss measured from the OTDR trace is less than 5 dB. One explanation for this disparity might be the nature of the microbends themselves. A corrugated plate with at least 40 sharp V-grooves was used by Reference 3, while only four piano wires, each 178 μm in diameter, were used in this study to produce the microbends. We observed very small peaks similar to Reference 3 when a corrugated plate was used. The resulting enhancement of backscattering was not quantifiable. It is important to note that there was no explanation given for the backscattering enhancement in Reference 3, which dealt with the modal power distribution of the backscattered trace from microbends.

The peak levels are presented and fitted with a cubic spline curve in Figure 7.3. When the displacement is smaller than 0.2 mm, there is appreciable loss, but little or no peak. Traditional microbending sensors, which rely on loss measurements only, operate at distortion levels smaller than the diameter of the fibre. To produce sufficient loss for small amplitudes, more microbend periods are necessary. In our experiments, fewer periods were found to produce better peaks for lower losses. The losses are plotted against the peak levels in Figure 7.5. It is seen that the PDR of the peak is less than 0.35 for an 80% transmission loss.

An effort to study the relationships between the peak level and the number of periods and the periodicity failed due to high levels of fluctuations in the backscattered trace that drowned any trends, if present. However, it appeared that the enhancement of backscattering takes place at the very beginning of the microbend region and the following periods contribute only to the losses.

In search of a cause for the backscattering enhancement, the possibility of power coupling between forward and backward propagating modes due to the curvature spectrum of the microbend was investigated. For a sinusoidal profile of the bend region, this was found to be impossible due to the large modal separation of the nearest guided modes in the opposite directions. After careful consideration of the effects of refractive index variation due to stress[39-41], the coupling of power due to periodic stress in the core of the fibre was also discounted as a source of the backscattering enhancement.

7.2 SINGLE BENDS ON AN ELASTIC FOUNDATION

To test a hypothesis that the enhancement originates in the sharp entry into the bend, efforts were made to reproduce the peak from a simple bend profile. A corner bender was used to bend the fibre at various angles from 0° to 45°. The radii of curvature of the bends at the corner were estimated to be between 3 and 5 mm. The 45° bend, which produced a transmission loss of 0.4 dB, showed a very faint indication of a peak in the backscatter trace.

When a small radius loop was formed, the backscatter trace showed a definite peak at the expense of a large loss. For a 2 cm diameter loop, the loss was in excess of 3.5 dB, and the peak produced was 4.7 dB above the initial backscatter level. Similar effects have been reported before[10], but the cause was not investigated.

The fibre was pressed by a small diameter rod against a slightly tacky side of a double-sided adhesive tape on a soft foam foundation with surprising results. For a loss of only 0.5 dB, the enhanced backscattering produced was 7.5 dB higher than the initial level. The rod diameter was 2.35 mm and a 150 gm weight was used to bend the fibre. When the fibre was placed on the plain side of an adhesive note paper, but all other parameters were the same, the peak was reduced to 4 dB above the initial level. The peak totally disappeared when a soft mylar was used as the bending surface. The bender was set up for investigation of single bends to expand on these observations, the results of which are discussed below.

7.2.1 Effect of different surface types

Two sets of measurements were taken for the same fibre, rod diameter, and foam foundation. The only variable was the type of surface that was adhered onto the foam. In the first set of measurements, the fibre rested on the plain side of an adhesive note paper. In the second set of measurements, a double-sided adhesive tape was used as the bending surface. The side with the permanent adhesion was towards the foam surface, and the fibre rested on the slightly tacky side, where it could be easily repositioned. The diameter of the rod was 2.35 mm in both cases, and the average power in the fibre was adjusted to be the same.

The analysed data are presented in four plots. Figure 7.6 presents the peaks levels for different displacements of the bender. Losses calculated from the power meter and the backscatter trace are displayed in Figures 7.7 and 7.8, while the peaks are plotted against the corresponding losses in Figure 7.9 for comparative study. There is a remarkable difference in the slope of the curves. The peak levels rise sharply for a given loss when the fibre is resting on the adhesive surface, while the peaks stay below 0.5 PDR for the plain surface.

Photographs, presented in Figure 7.10, that were taken during this session reveal one probable reason for the large discrepancy between fibre behaviour on the two surfaces for two comparable data sets whose results are presented in Table 7.1.

Table 7.1 Effect of the surface on which the fibre is placed

Surface	Displacement	Peak	Loss
plain paper surface	2.51 mm	0.40	0.39
adhesive paper surface	2.4 mm	0.78	0.20

The photographs for these two data sets reveal a difference in the shape of the bend produced on the two surfaces. In Figure 7.10a, the white curve is the profile of the paper surface, and the fibre is the faint outline with a dark edge. The end of the bending rod is shown out of focus in the centre of the photograph. The left-hand side of the image, which is towards the OTDR, shows the fibre curving above the paper surface. In Figure 7.10b, the adhesion provided by the tacky side of the paper keeps the fibre touching the surface and provides a smoother shape. A plot of the fibre shapes is presented in Figure 7.11, where it is confirmed that the fibre is indeed bent differently for the two surfaces. The shape near the bending rod could not be determined from the photograph, but it is assumed that the fibre follows the circular surface of the rod for a short length.

An insight into the backscattering enhancement process may be gained from these photographs and the plot. A fraction of the energy lost at the bend is scattered, most probably by the jacket and the surrounding medium, in various directions. Some of the light is captured into higher order guided modes propagating in the backward direction. Since the attenuation is severe for these modes, any perturbation in their path causes re-radiation of the captured light. The shape of the fibre immediately

preceding the bend has a marked effect on the level of the enhanced backscattering observed from a fibre microbend.

Since the shape of the bent fibre contributed to such a difference in the observed peak levels and losses, photographs illustrating the shape for several sensor displacements were taken, and are presented in Figure 7.12. The values of the peak and loss for each shape are shown below the photographs for comparison. Since the diameter of the bending rod was 2.35 mm, the maximum amplitude of the bend profile does not increase after a bender displacement of 2.35 mm has been applied; only the shape changes. The first three shapes could be fitted with inverse hyperbolic cosine curves of the form A/cosh(Bz) within the visual reading error. The fourth shape could not be represented with such a curve within the error bounds. The inverse hyperbolic cosine function was higher than the bend profile for large values of z, and lower than the profile for small values of z. The inflection of the actual bend profile occured close to the FWHM point.

7.2.2 Effect of the bend profile

Since the shape of the bent fibre was deemed to have an influence on the backscatter enhancement, an effort was made to produce different shapes by pressing the fibre with different diameter rods. The double-sided adhesive paper was used throughout these experiments. The rod diameters used were 2.35 mm and 1.55 mm.

The analysed data are presented in four plots. Figure 7.13 presents the peak levels for different displacements of the bender. Losses calculated from the power meter and the backscatter trace are displayed in

Figures 7.14 and 7.15, while the peaks are plotted against the corresponding losses in Figure 7.16 for comparative studies. In general, the smaller diameter rod produced larger backscattering enhancement for similar displacements. However, the diameter of the rods were different, so a direct comparison between the bend profiles created by the two rods is difficult to make. The losses were marginally smaller for the smaller diameter rod, which may appear paradoxical. However, the contact regions under the bending rods will have different lengths depending on the diameter of the rods, the displacement, and elasticity of the surrounding medium. The total loss is the result of the total length, and the radius of curvature of this region. So it may be possible to achieve smaller losses with the smaller diameter rod.

There is a small discrepancy in Figure 7.13 in the last data points for the small diameter rod. The peak level appears to be slightly smaller for a larger sensor displacement, while the loss, presented in Figure 7.14, is higher. Although the peak levels are within the error bounds of the plot, in all other experiments, the observed peak levels have increased or saturated for increasing bender displacements. These two points presented enough anomaly to warrant further investigation. The photographs of the fibre taken during these two experiments are presented in Figures 7.17. There is no appreciable change in the fibre shape between the two photographs. It was speculated that the soft foam required some time to distribute the forces after a increase in displacement. During the last measurement, the foam failed to respond to the applied force and adjust the shape of the fibre. The fact that for the same profile of the fibre, the peak level did not change appreciably, but the loss did, corroborates two of our assumptions. The bend

profile is an important modulator of the backscattering enhancement, but not for the loss. Most of the loss should occur in the contact region with the rod at the centre of the bend. This conclusion is also consistent with our hypothesis that the backscatter enhancement is caused by the capture of a fraction of the energy lost at the bend into leaky and higher order guided modes in the backward direction. These modes are prone to re-radiation immediately after capture, but gradually become better guided after traveling a few millimeters. The principal modulator of the observed peaks will be the profile of the fibre towards the OTDR end of the fibre. The full width at half maximum (FWHM) of the bend profiles are plotted for various displacements in Figure 7.18, and the peaks and losses are plotted against the FWHM in Figure 7.19. The FWHM decreases rapidly and then approaches an asymptotic value. The elasticity of the medium and the flextural rigidity of the fibre will determine this value. The PDR of the peaks are near unity for FWHM < 5 mm.

The power meter and the backscatter trace showed increasing loss for increasing displacements. The area of contact was not visible in the photographs, but the length of the fibre conforming to the rod diameter is conjectured to be more dependent on the sensor displacement and the rod diameter than on the elasticity of the surrounding medium, while the profile of the fibre before and after this contact region would depend more on the elasticity of the surrounding medium. It could be deduced that most of the loss occurred at the very small region of the fibre in contact with the rod. The loss data plotted in Figure 7.14 indeed show a slight trend of more loss for the larger diameter rod. This result is not paradoxical, since a larger length of fibre is in contact with the larger diameter rod for large

displacements of the sensor. Although the loss per unit length is smaller for the larger diameter rod, the increased contact length produces more aggregate loss for the bend. Based on the observations and discussion from the previous experiments, an idealized depiction of the generation of the enhanced backscattering is presented in Figure 7.20.

7.2.3 Hysteresis effect of the elastic foundation

The deviation from perfectly elastic behaviour of the foam foundation was found responsible for an inconsistency in the bend profile in the discussion of the previous section. In the following sets of experiments, a 'hysteresis' effect was observed when the displacement was gradually decreased after a maximum displacement was applied to the bender. The fibre was pressed against an adhesive paper tape with a 1.55 mm diameter rod. Figure 7.21 presents the peaks levels for various displacements of the bender. Losses calculated from the power meter are displayed in Figure 7.22. The hysteresis effect is apparent in both figures. Two photographs of the bent fibre for the same sensor displacement but for increasing and decreasing displacements of the bender is presented in Figure 7.23. The width of the profile is larger in the reverse direction for the same bender displacement, resulting in smaller peaks, when the stress is gradually removed from the foam foundation. The cause of this 'hysteresis' effect is the gradual creep in the foam after a large stress has been applied. When the force is removed, the stress is reduced at a faster rate as a result of this effect.

7.2.4 Effect of the removal of the fibre jacket

A possible explanation for the backscattering enhancement presented in Figure 7.20, is that the enhancement occurs when some of the energy radiated from a bend is captured in the backward propagating modes after scattering in the surrounding medium. To prove this hypothesis, further study of the effect of the surrounding medium was required. The jacket material of the test fibre was urea acrylate, extending from 62.5 μm to 250 μm from the centre of the fibre core. Since the ultraviolet-cured urea acrylate coating of the fibre is not optimized for light propagation, it was speculated that the jacket material presented a significant scattering medium in the immediate vicinity of the bend region.

The effect of the jacket material on the backscattering enhancement was studied by carefully stripping a roughened section of the fibre jacket using a methylene chloride solution. The fibre was carefully placed on a double-sided adhesive tape, and bent using a 1.55 mm diameter rod. The result of this experiment is presented in conjunction with the result of bending the jacketed fibre at a region 10 cm away under similar conditions.

The analysed data are presented in four plots. Figure 7.24 presents the peaks levels for different displacements of the sensor. Losses calculated from the power meter and the backscatter trace are displayed in Figures 7.25 and 7.26, while the peaks are plotted against the corresponding losses in Figure 7.27 for comparative studies. The removal of the jacket placed the core of the fibre approximately 250 μm closer to the bending rod for the same displacement, so the bend profiles for the jacketed and the bare fibres were slightly different for comparable bender displacements. The loss

was slightly higher for the bare fibre when the same bender displacement was applied, which is consistent with the smaller bending radius. The backscattering enhancement is much smaller in the bare fibre, but it is still present at a significant level. Several photographs of the bare fibre and the jacketed fibre at various stages of bending are presented in Figure 7.28. The conjecture is that the outer edge of the fibre is in intimate contact with the white paper tape, and thus the radiated light can still be scattered back into the fibre.

In an effort to reduce the effect of the paper tape on which the fibre was placed, various coatings were applied to the bare fibre. When the fibre surface, the paper surface and the bending rod were thickly coated with black enamel paint to reduce any scattering of light, the peak levels were still present. Reflective aluminum paint produced slightly larger peak levels, and lower losses, than did the metallic black paint. The peaks and losses for these two studies are presented in Figures 7.29 and 7.30. The study was not conclusive due to a lack of knowledge about the composition and distribution of the metallic particles in the sprayed paint, and their optical properties at 850 nm wavelength. The best assumption we could make was that the coating was essentially in the form of a dried emulsion with suspended metallic particles that formed many scattering centres distributed randomly on the surface of the fibre.

Total suppression of the enhanced backscattering was achieved by liberal use of a permanent black felt pen on the fibre and other surrounding material. The photograph of the fibre just before breakage is presented in

Figure 7.31 along with the photograph of a comparable bend profile for a jacketed fibre.

7.2.5 Overall comparison

The ideal distributed sensor element should have the lowest losses to produce the highest levels of enhanced backscattering. For overall comparison, the peak levels are plotted against the losses for various bender configurations in Figure 7.32. A regular fibre placed on a slightly adhesive paper surface on an elastic foundation and pressed with a 1.55 mm rod produced the best performance figures in terms of the peaks produced for given losses. The 2.35 mm rod also produced comparable results. The periodic microbends gave the worst performance. A bare fibre placed on the same adhesive paper produced better performance than both periodic microbends and a jacketed fibre placed on a non-adhesive paper surface. When the bare fibre was coated with metallic enamel sprays, the backscattering enhancement was larger. Since coating the fibre with a permanent black felt pen reduced the peaks to zero, there is no curve in Figure 7.32 to account for this situation.

The comparison between the bare fibre resting on the adhesive surface, and the jacketed fibre resting on the plain paper brings into question the assumption that most of the scattering is produced in the jacket when it is present. It is possible that the paper surface itself, rather than the shape of the fibre produced the extra backscattering. The adhesive coating was initially colorless and even across the surface, but changed to a muddy grey color and formed slight clumps after repeated use. No random

microbending losses were detected due to the clumps of adhesives. The maximum possible contribution from the paper or the adhesive coating should be the backscattering enhancement that was observed when the bare fibre was placed against the adhesive surface. When the jacket is present, the attenuation due to the two-way propagation and scattering in the jacket may reduce this contribution significantly.

7.2.6 Investigation of bends in series

Using a 30 cm long strip of foam placed on a table, a simple investigation of distributed sensing was undertaken. The fibre was placed on an adhesive paper surface and pressed with several 1.55 mm diameter rods simultaneously at several locations. Figure 7.33 presents the backscatter trace for three equal forces on the fibre, each approximately 10 cm apart. The backscattering peaks are progressively lower due to the effect of the preceding bends. The forces were applied by placing 200 gm-wts on the rods.

The effect of varying the forces are presented in Figure 7.34.In one trace, the first and second locations were pressed with 150 and 200 gm-wts respectively. The trace obtained after 50 gm-wts were removed from the first location shows that the change in the enhanced backscatter peaks are much larger than the change in the loss levels. The traces are plotted in Figure 7.35a as decibels above or below the initial Rayleigh backscattering level. The change in the loss levels are drowned in noise, while the change in the peak level is apparent. A dynamic smoothing algorithm was applied to the backscattered trace to reduce the noise levels while retaining the peak

levels. The result is presented in Figure 7.36 to show the added clarity that can be achieved by additional signal processing.

To demonstrate the feasibility of simultaneously detecting multiple bends, software were written to scan the fibre in the region where the fibre was placed on an elastic foundation. Various small diameter rods were used to press down the fibre anywhere within this region. The OTDR averaging rate was set at 256 pulses per location, but could be varied. An algorithm was developed to detect multiple pulses from this noisy data and display their locations and heights. The time for each scan was less than a second, while the calculations were performed in milliseconds by a 12 MHz PC-AT. The algorithm successfully resolved multiple peaks separated by at least 5 cm, and the location of single peaks were determined with an accuracy of less than a centimeter. During an open house at the Laser Institute, this system operated continuously for 8 hours per day in an unattended mode. Occasionally, there were communication errors, but the data acquisition software was designed to reset after such an error. Otherwise, every attempt to press the fibre with greater than 50 gm-wt for longer than a second was detected. This simple demonstration illustrated the possibility of developing real-time distributed sensors using enhanced backscattering.

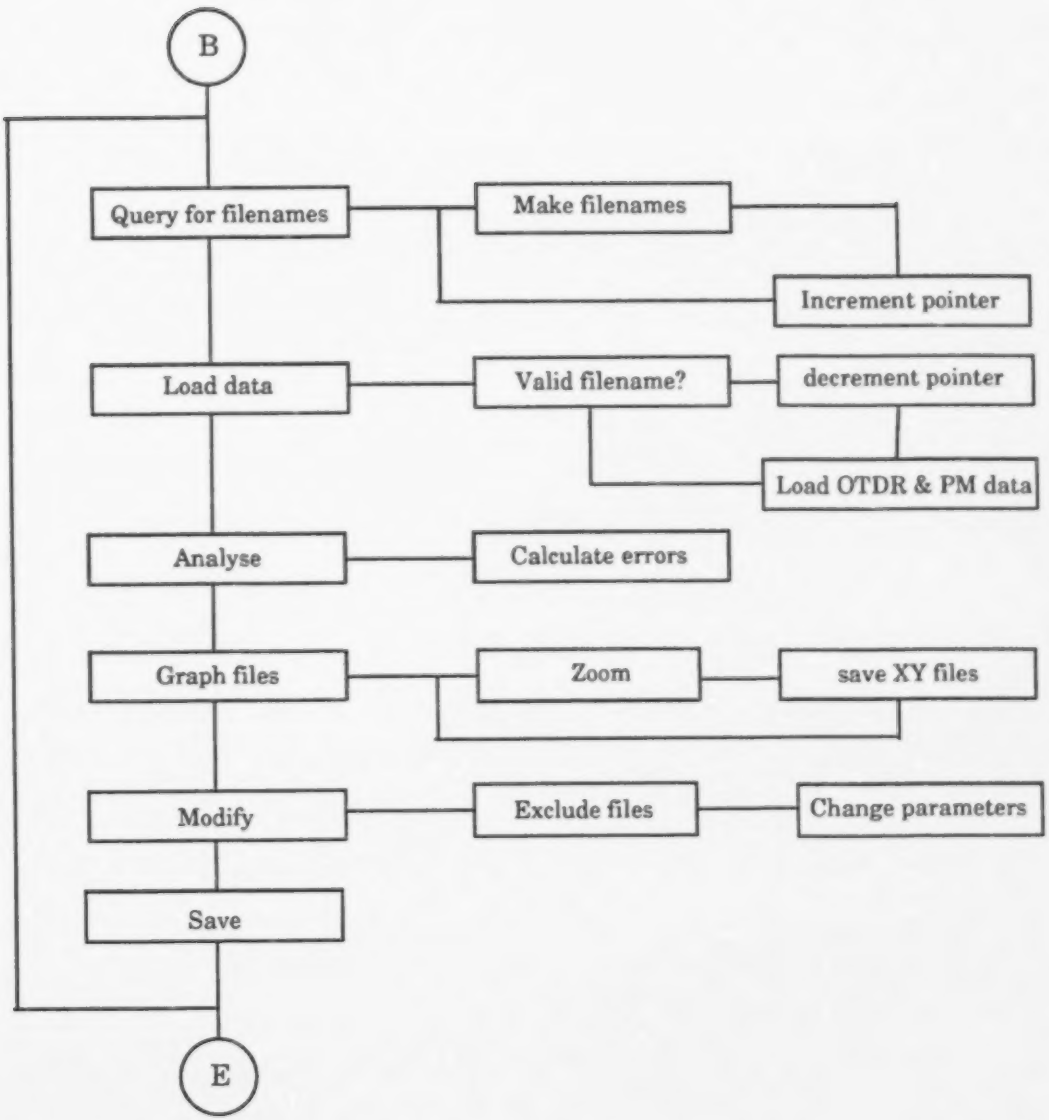

Figure 7.1 Flow diagram of data analysis software.

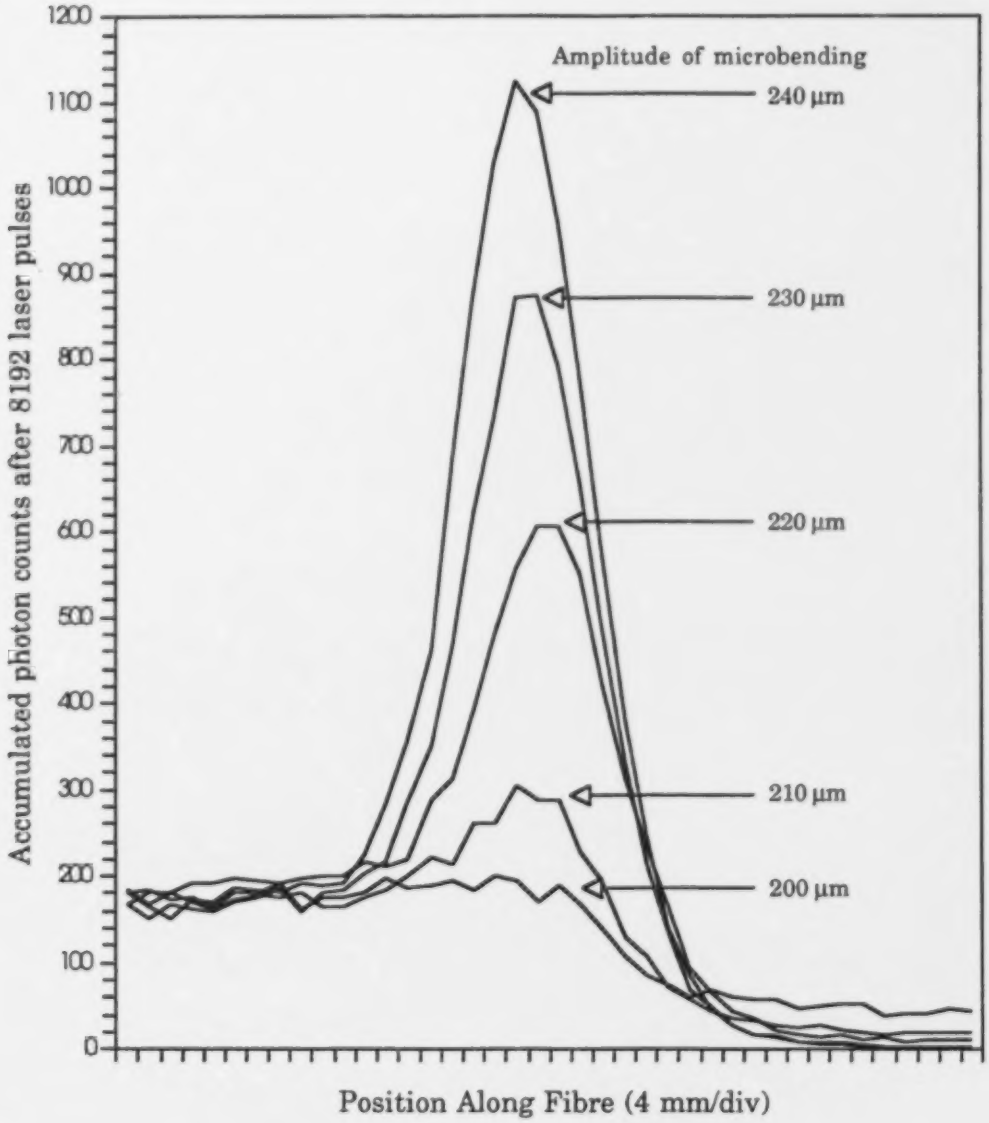

Figure 7.2 Backscatter enhancement from periodic microbends.
(Λ = 1.15 mm; 4 periods)

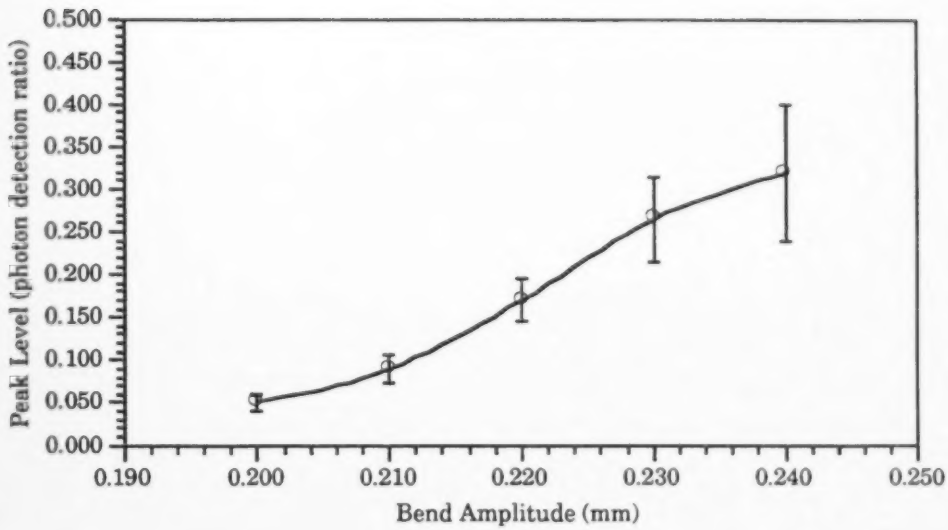

Figure 7.3 Peaks of the enhanced backscattering at various microbending amplitudes.

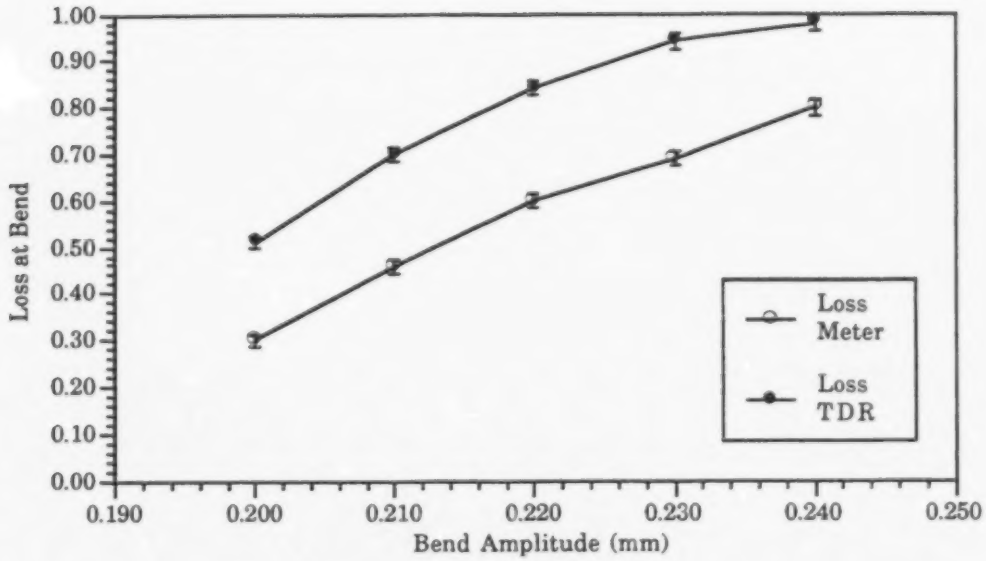

Figure 7.4 Losses produced by periodic microbending.

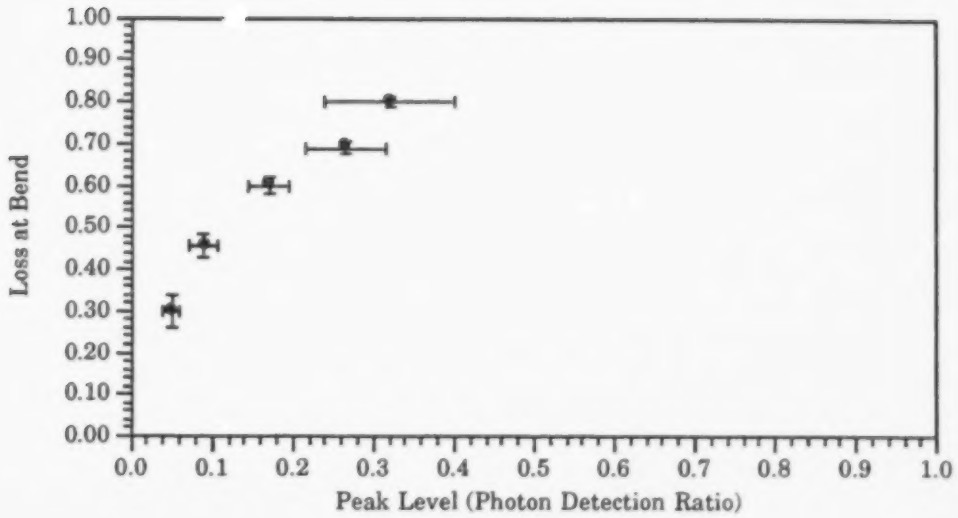

Figure 7.5 Comparison between the loss and peak levels produced by the same microbending distortion.

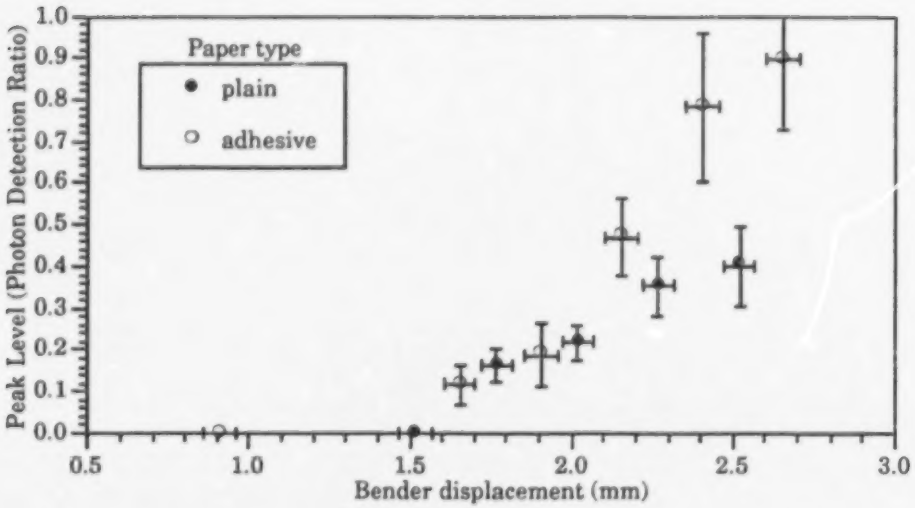

Figure 7.6 The peaks produced by resting the fibre on two different paper surfaces on a foam foundation.

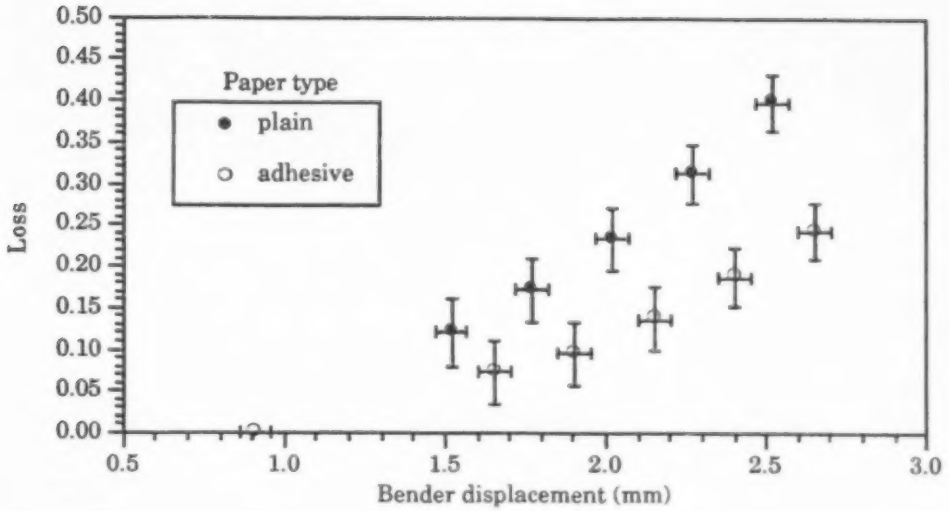

Figure 7.7 The (power meter) losses due to bending the fibre on two different surfaces.

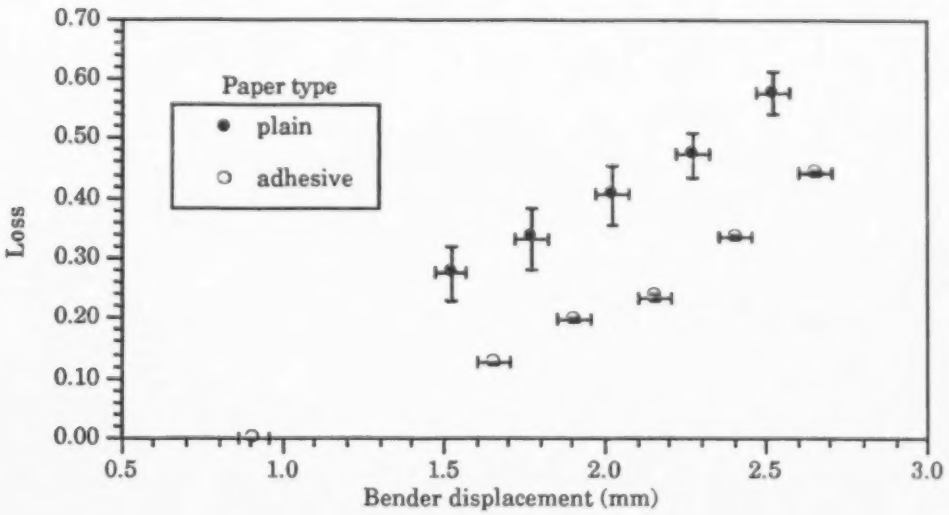

Figure 7.8 The (OTDR) losses due to bending the fibre on two different surfaces.

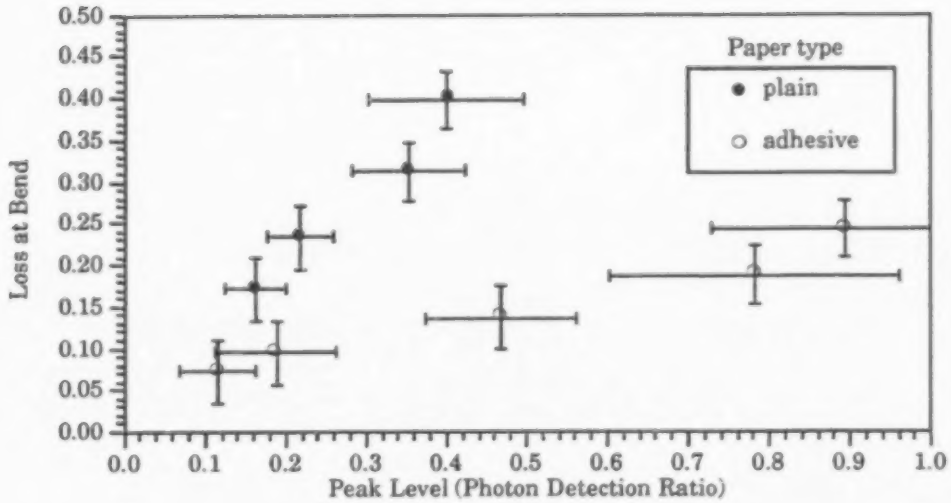

Figure 7.9 Comparison of the peaks against the losses due to bending the fibre on two different surfaces.

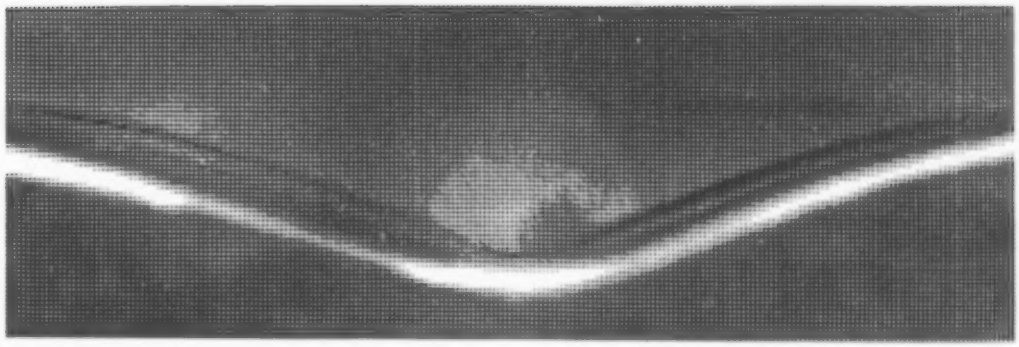

a: (plain surface; bender displacement: 2.51 mm; peak: 0.4; loss: 0.4)

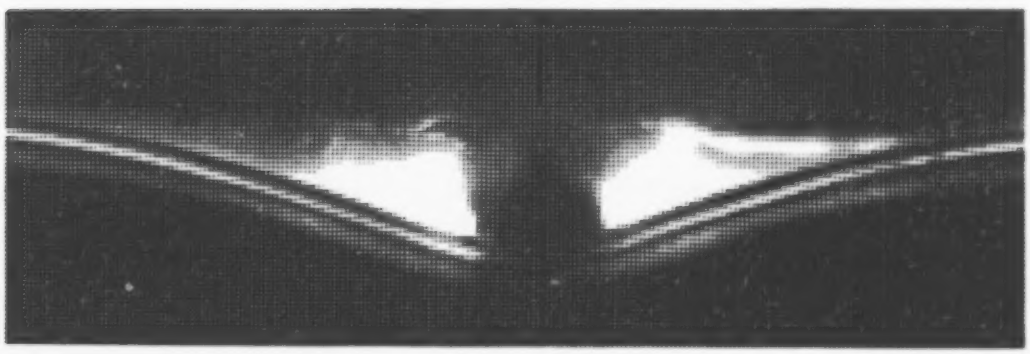

b: (adhesive surface; bender displacement: 2.4 mm; peak: 0.8; loss: 0.2)

Figure 7.10 Bend shapes on two different surfaces.

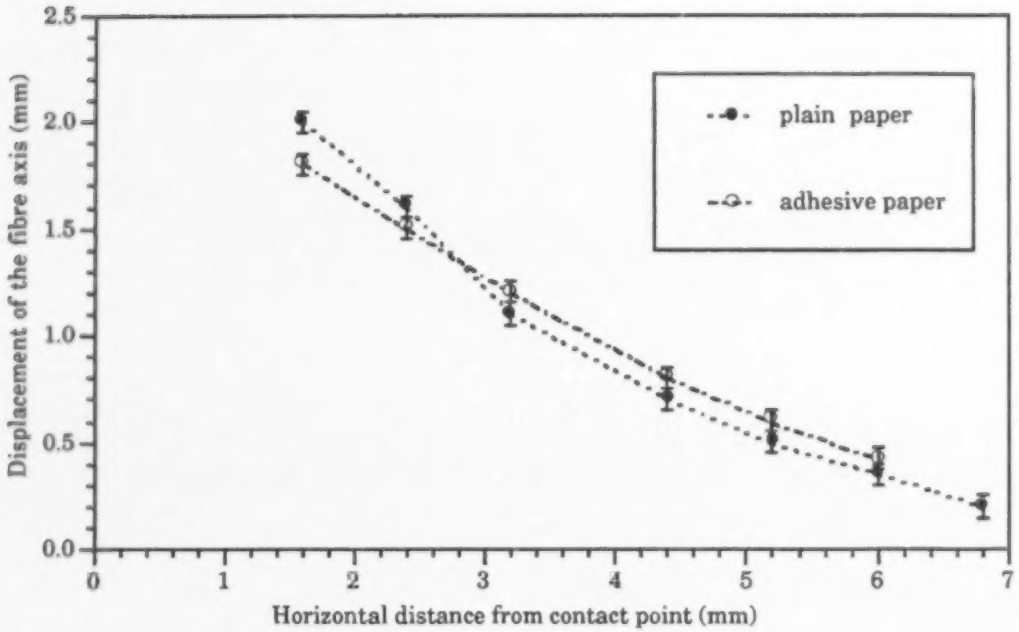

Figure 7.11 Comparison of the shape of the bend on two different surfaces.

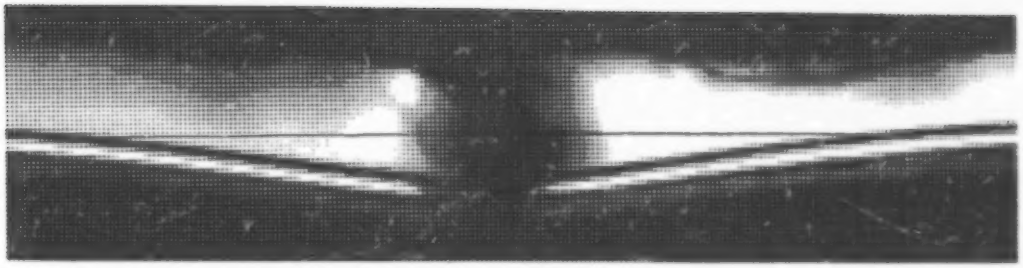

a: (bender displacement: 0.9 mm; peak: 0.0; loss: 0.03)

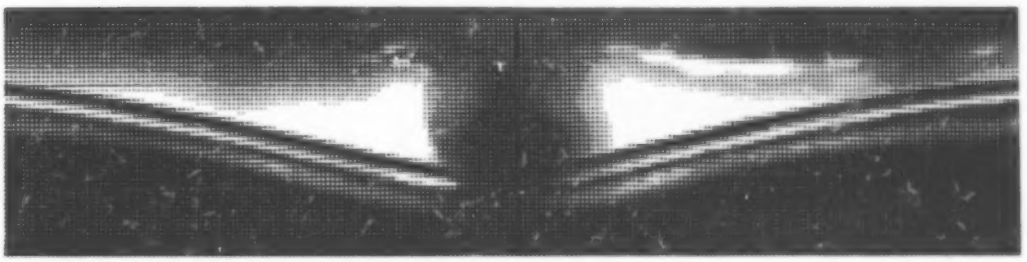

b: (bender displacement: 1.7 mm; peak: 0.2; loss: 0.10)

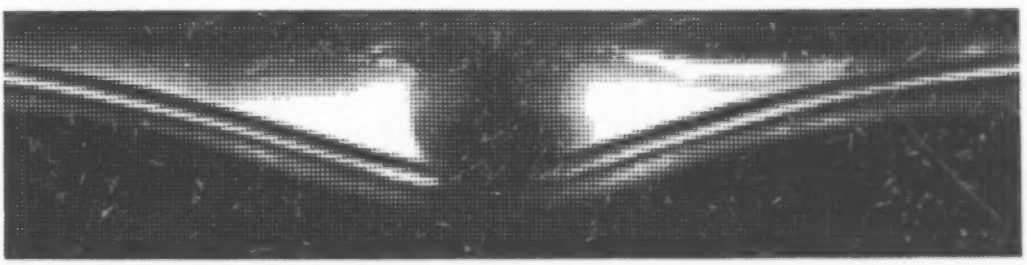

c: (bender displacement: 2.2 mm; peak: 0.5; loss: 0.13)

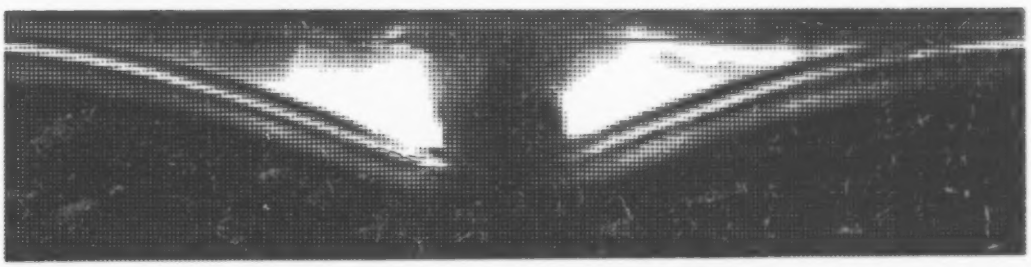

d: (bender displacement: 2.65 mm; peak: 0.9; loss: 0.24)

Figure 7.12 Photographs of the bend profiles for increasing bender displacements. (Rod dia: 2.35 mm; adhesive surface)

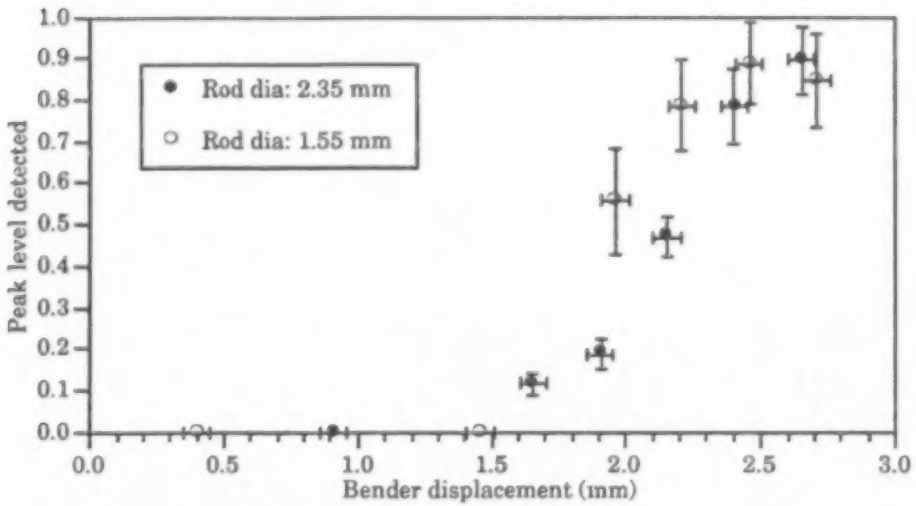

Figure 7.13 The peaks produced by two different rod diameters.

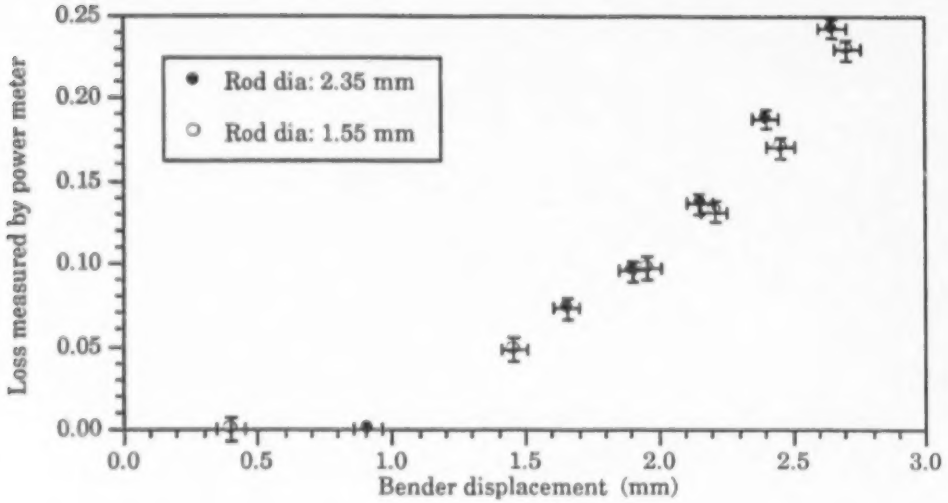

Figure 7.14 The (power meter) losses produced by two different rod diameters.

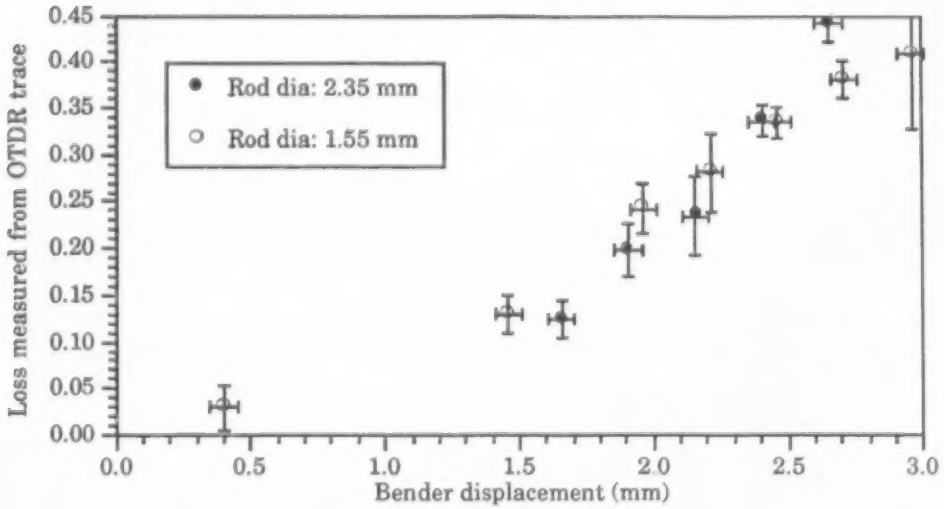

Figure 7.15 The (OTDR) losses produced by two different rod diameters.

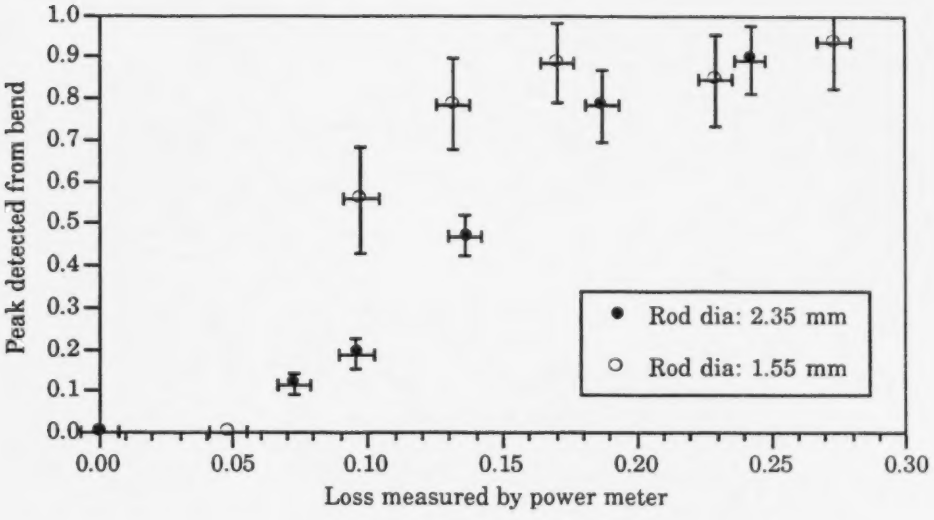

Figure 7.16 Comparison of the peaks against losses for to two different rod diameters.

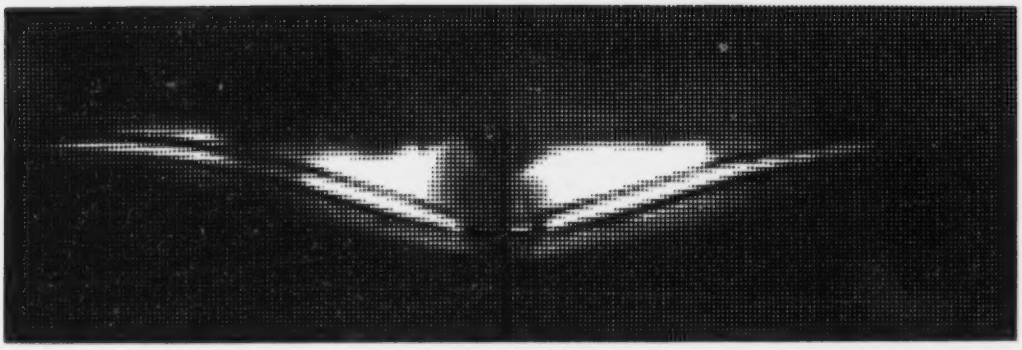

a: (bender displacement: 2.46 mm; peak: 0.88; loss: 0.17)

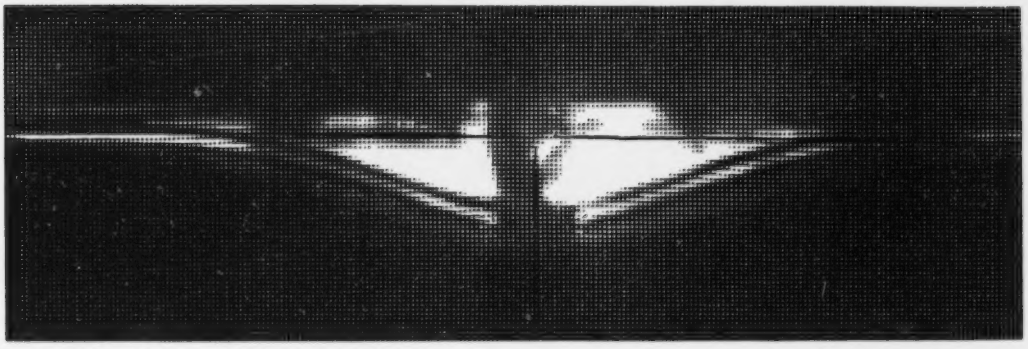

b: (bender displacement: 2.71 mm; peak: 0.84; loss: 0.23)

Figure 7.17 Similarity in the bend shape obtained for two different bender displacements.

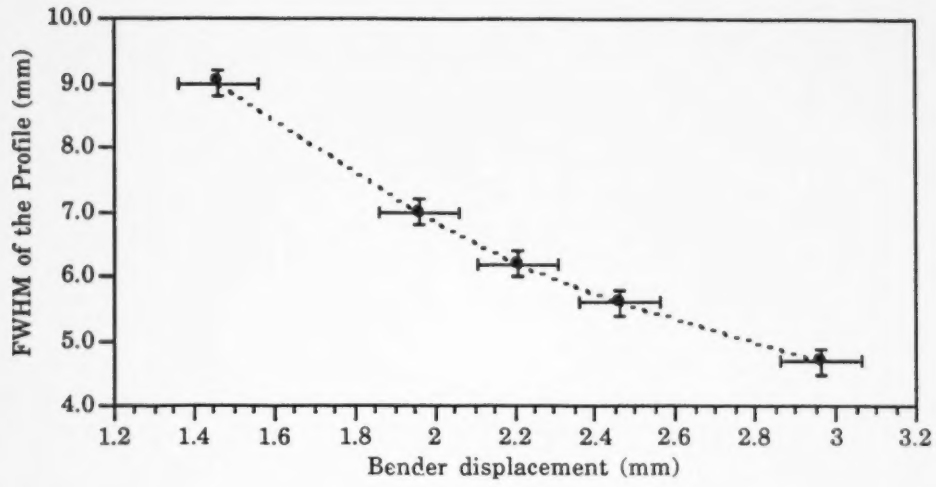

Figure 7.18 The relationship of the FWHM of the bend profile to the bender displacement.

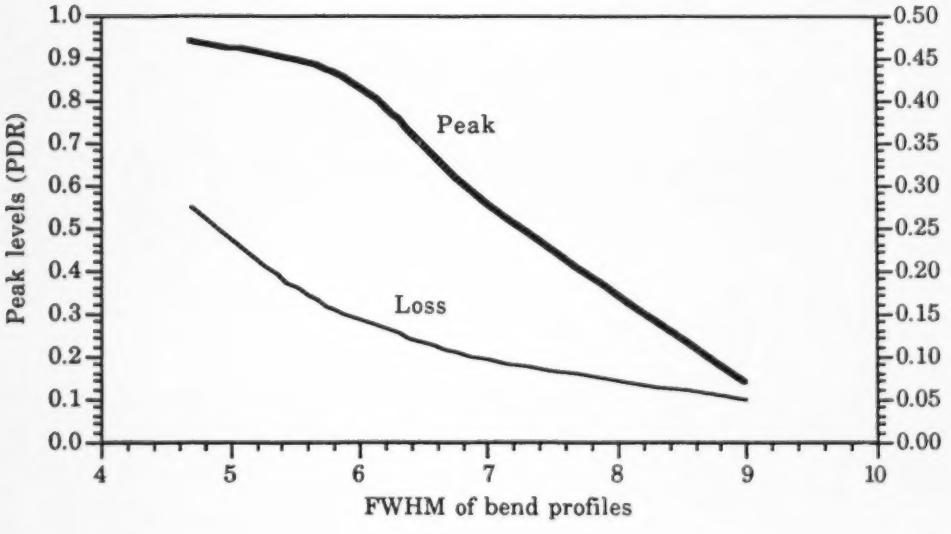

Figure 7.19 The relationship of the peak and loss to the FWHM of the bend profile. (The Y axis to the right is for the loss.)

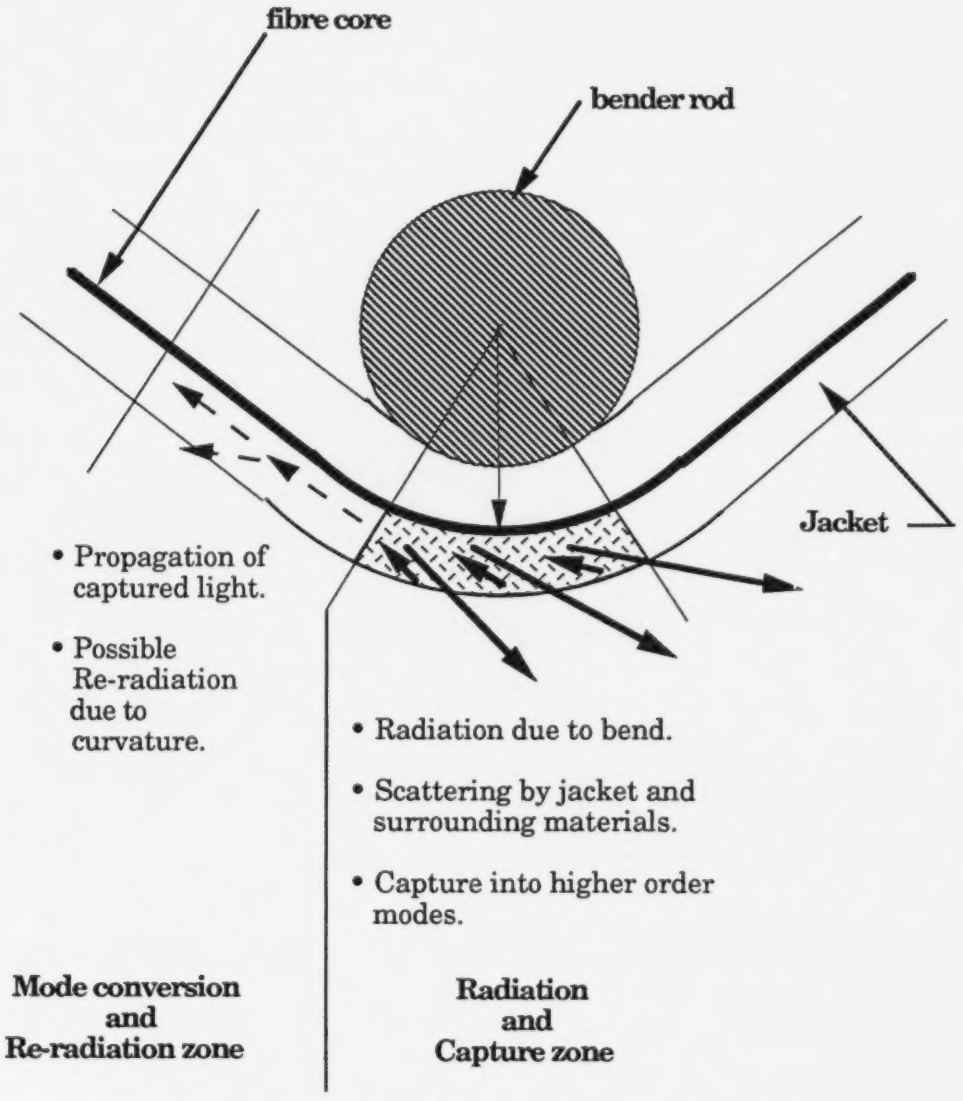
fibre core
bender rod
Jacket
• Propagation of captured light.
• Possible Re-radiation due to curvature.
• Radiation due to bend.
• Scattering by jacket and surrounding materials.
• Capture into higher order modes.
Mode conversion and Re-radiation zone
Radiation and Capture zone

Figure 7.20 A probable mechanism for the backscatter enhancement.

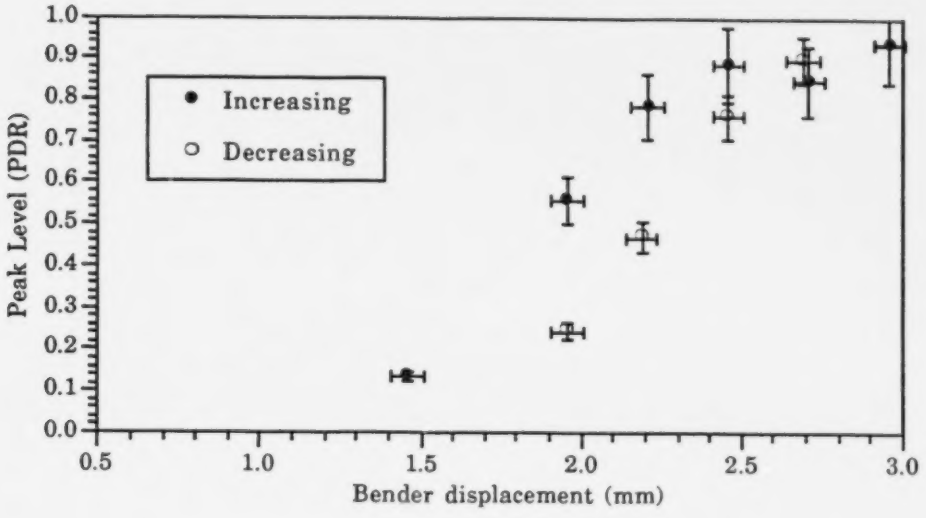

Figure 7.21 Observation of a 'hysteresis effect' on the peak when displacement is increased to a maximum and gradually decreased.

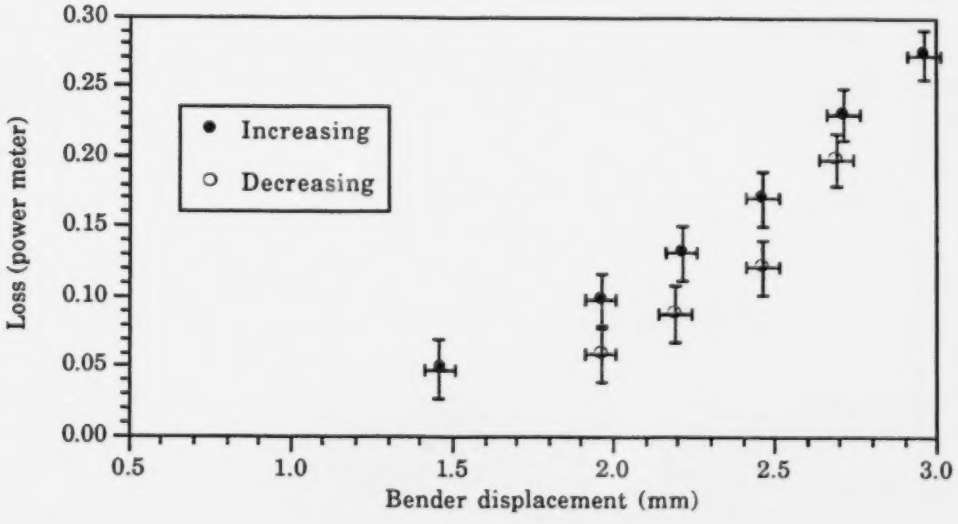

Figure 7.22 Observation of a 'hysteresis effect' on the loss when displacement is increased to a maximum and gradually decreased.

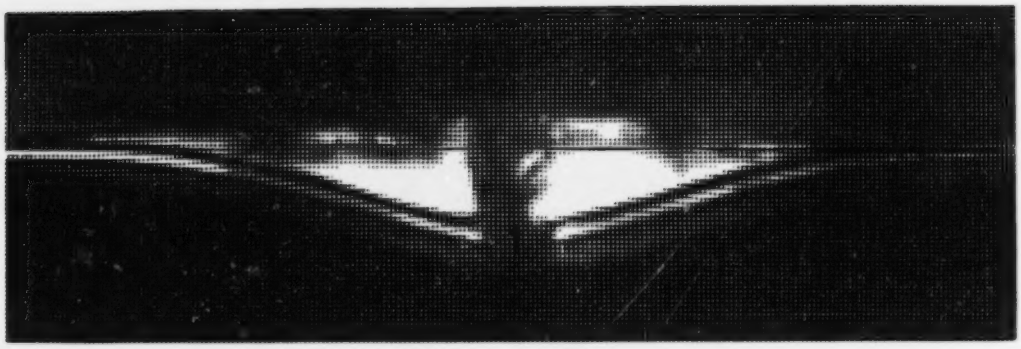

a: (bender displacement: 2.2 mm; peak: 0.8; loss: 0.13)
when displacements were increasing

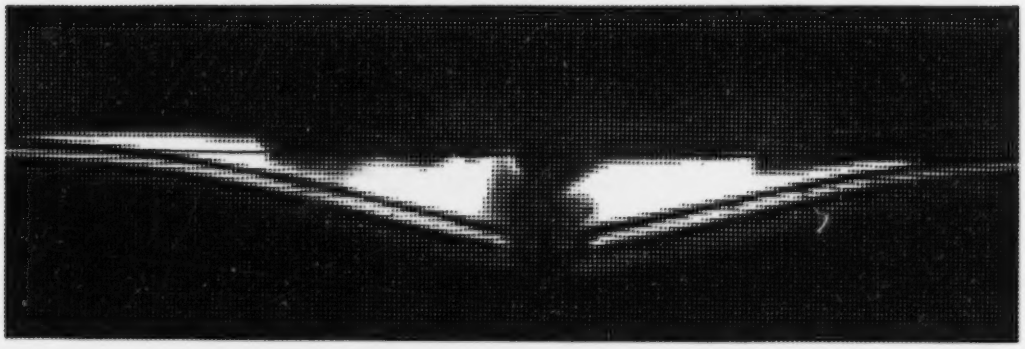

b: (bender displacement: 2.2 mm; peak: 0.5; loss: 0.10)
when displacements were decreasing

Figure 7.23 Difference in the shape of the fibre for the same displacement, but when the bender movement was in opposite directions.

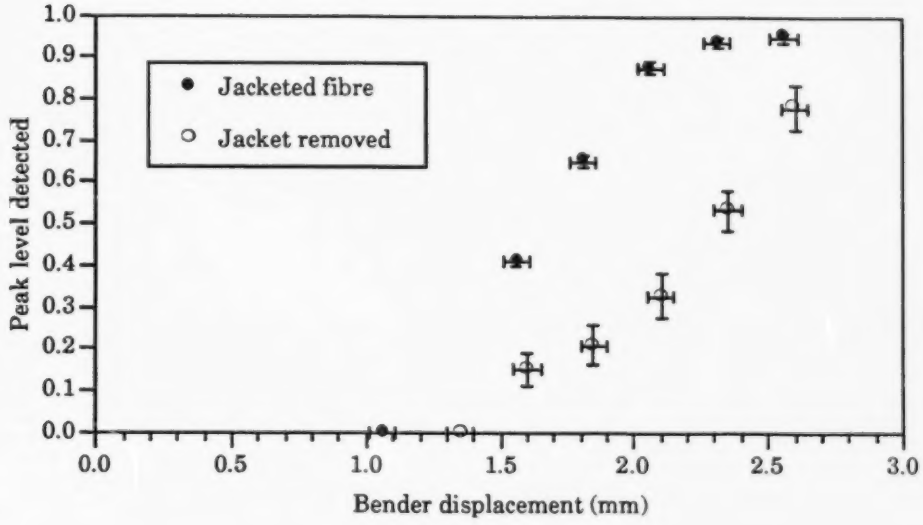

Figure 7.24 The peaks produced at different displacements for jacketed and bare fibres.

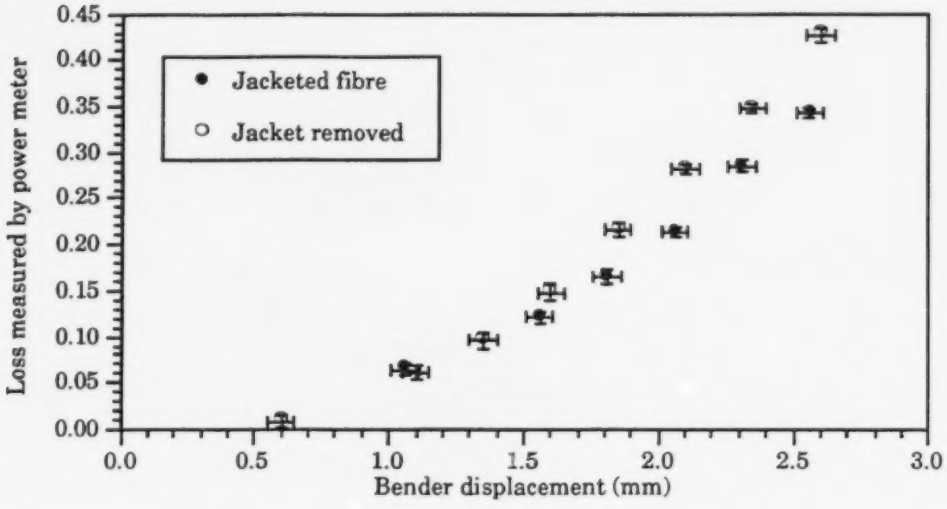

Figure 7.25 The (power meter) losses at different displacements for jacketed and bare fibres.

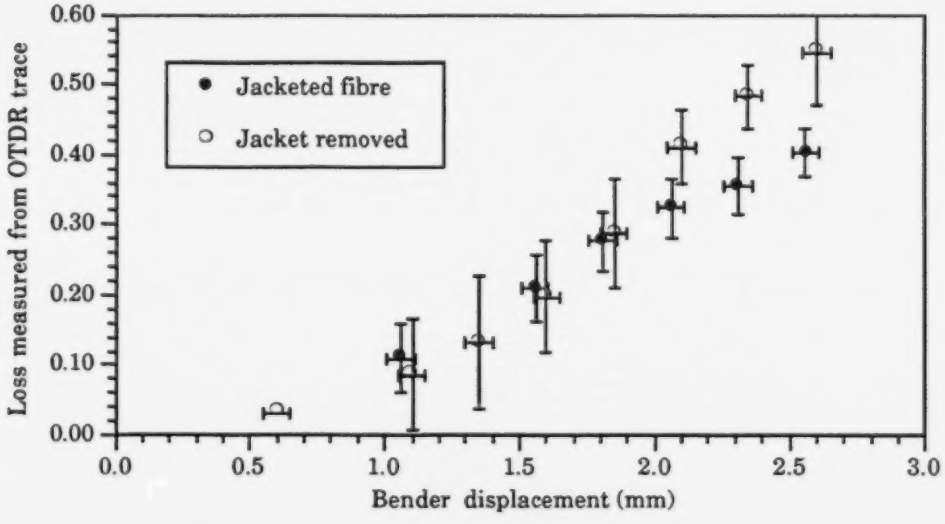

Figure 7.26 The (OTDR) losses at different displacements for jacketed and bare fibres.

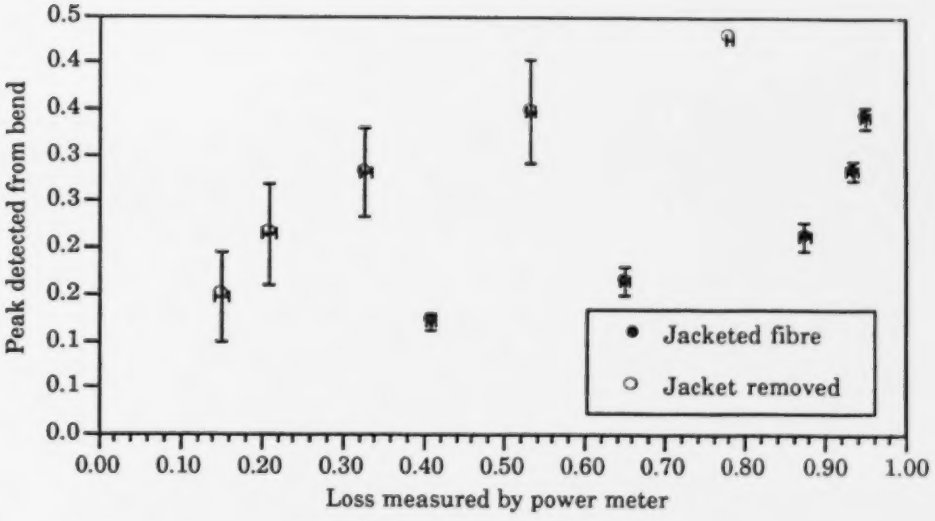

Figure 7.27 Comparison of the peaks against the losses for jacketed and bare fibres.

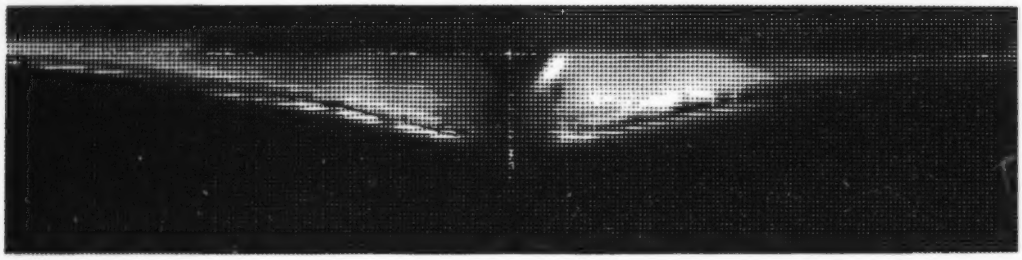

a: (bender displacement: 1.6 mm; peak: 0.15; loss: 0.15)

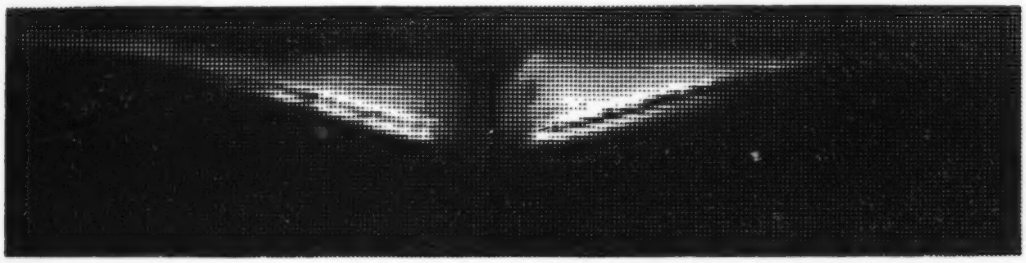

b: (bender displacement: 2.1 mm; peak: 0.33; loss: 0.28)

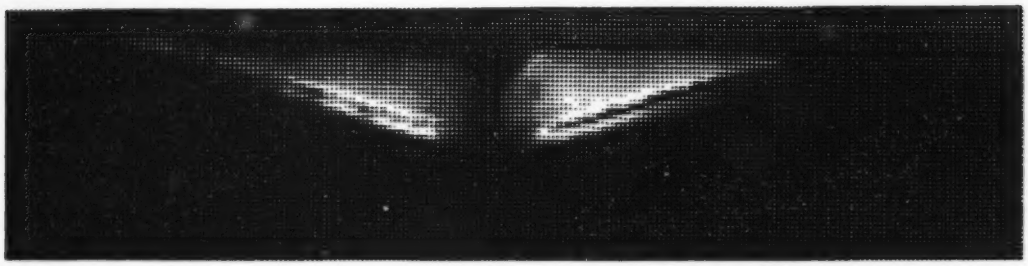

c: (bender displacement: 2.35 mm; peak: 0.53; loss: 0.35)

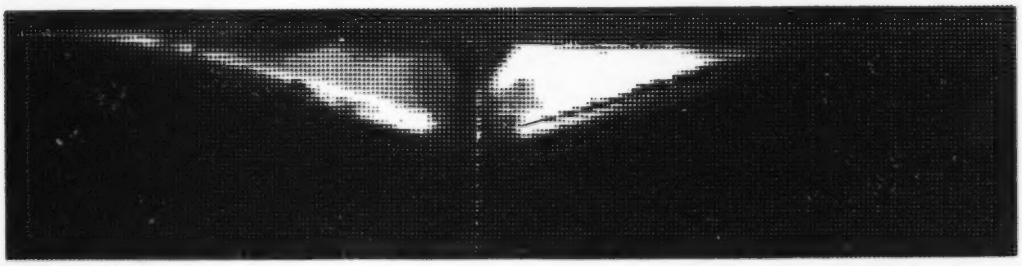

d: (bender displacement: 2.6 mm; peak: 0.78; loss: 0.43)

Figure 7.28 Bend profiles for a fibre whose jacket has been removed.

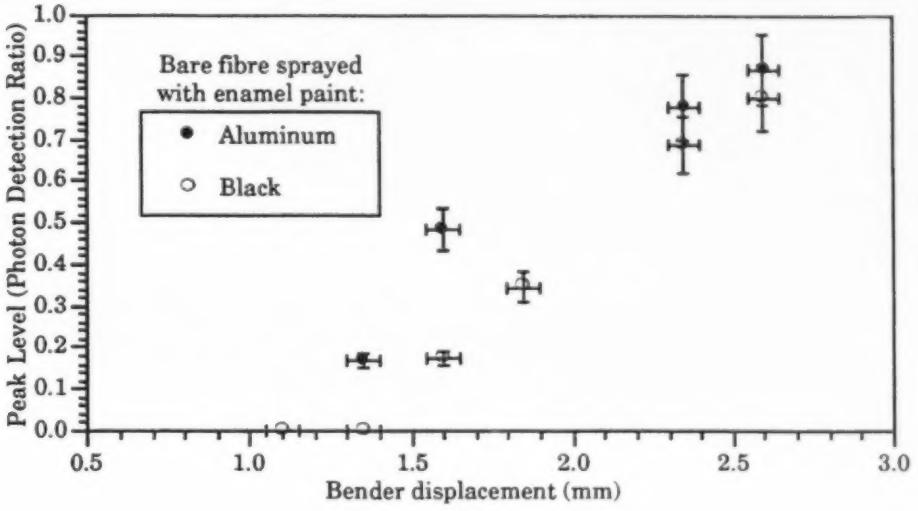

Figure 7.29 The effect of two different metallic sprays on the peak levels for a bare fiber.

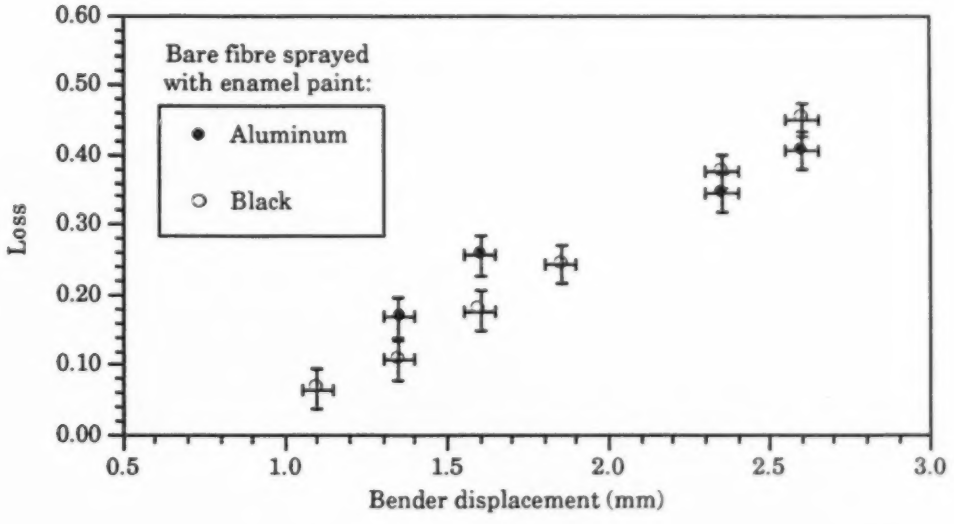

Figure 7.30 The effect of two different metallic sprays on the loss levels for a bare fiber.

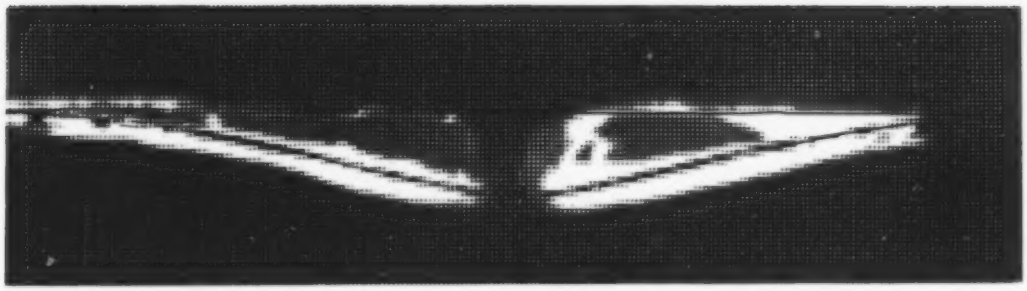

a: (fibre without jacket, painted with felt pen; bender displacement 2.2 mm; peak: 0; loss: 0.17)

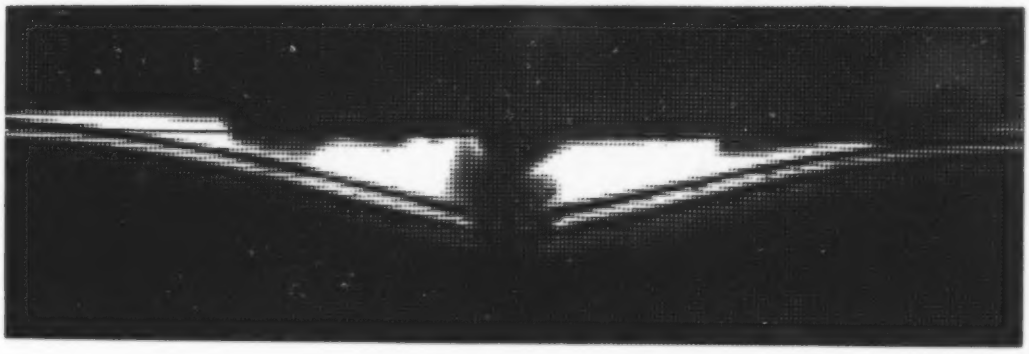

b: (jacketed fibre, comparable bend profile; bender displacement 2.2 mm; peak: 0.47; loss: 0.13)

Figure 7.31 The remarkable difference in the peak and loss levels for fibres with and without a jacket for a similar bend profile.

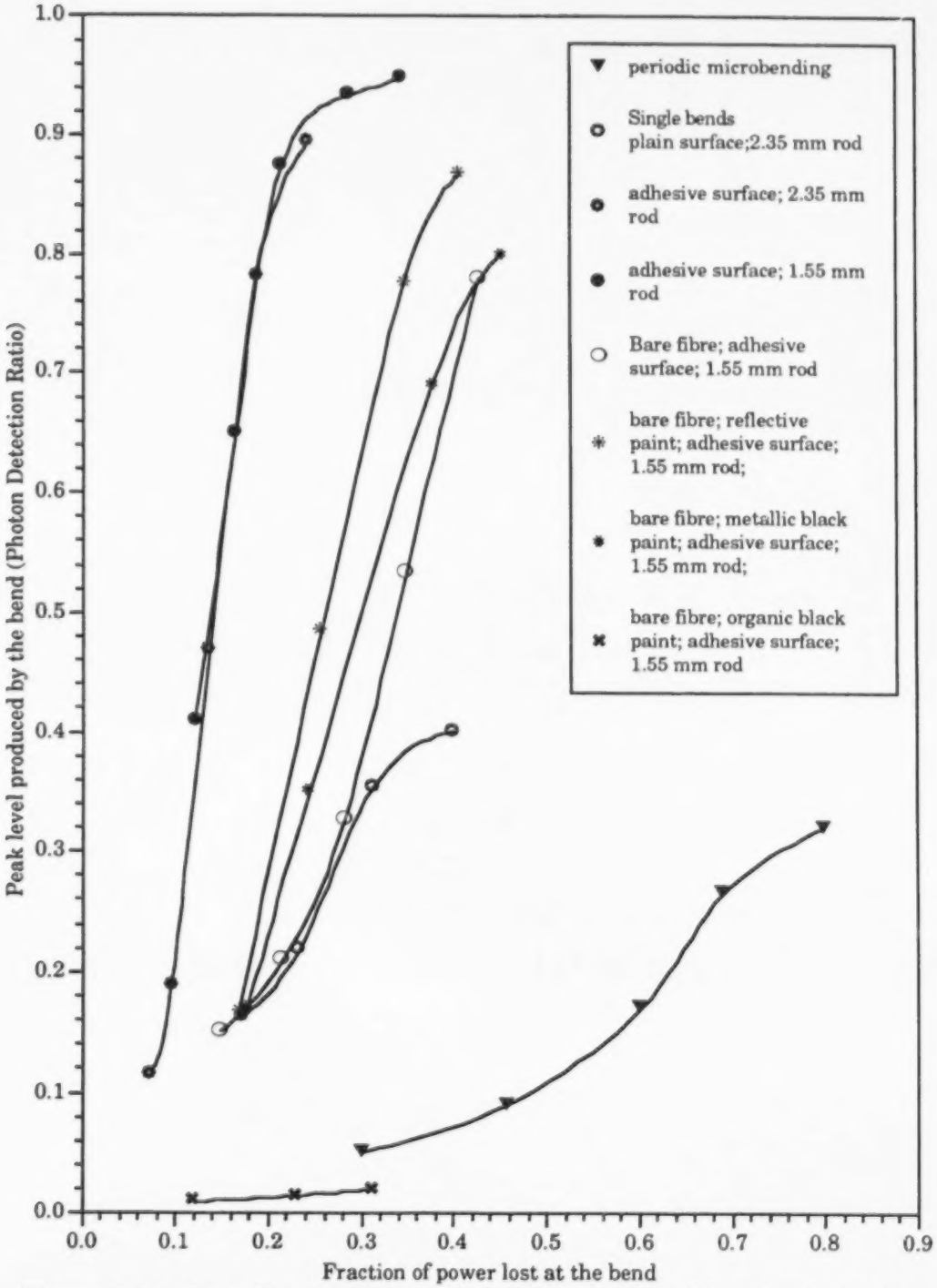

Figure 7.32 Overall comparison between the peak and loss levels for the experiments performed.

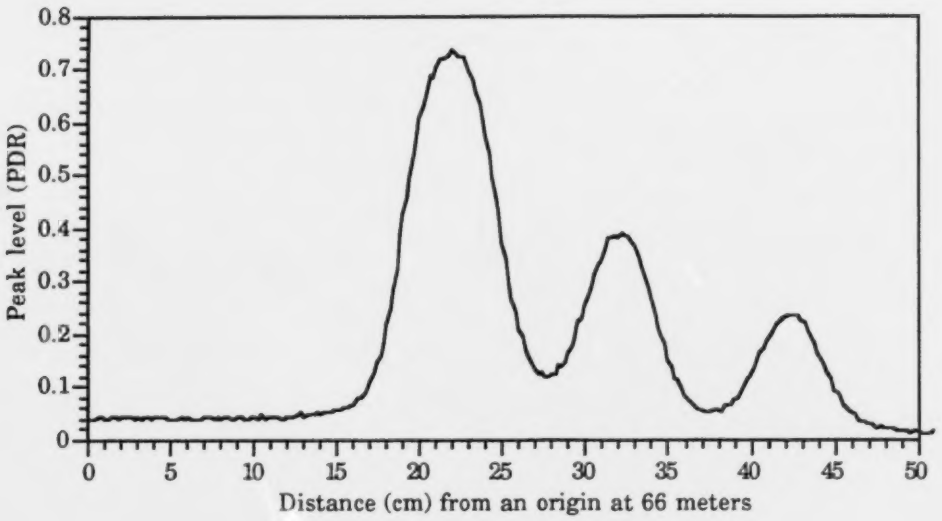

Figure 7.33 The backscattered trace showing enhancement peaks from three locations pressed by equal forces of 200 gm-wt.

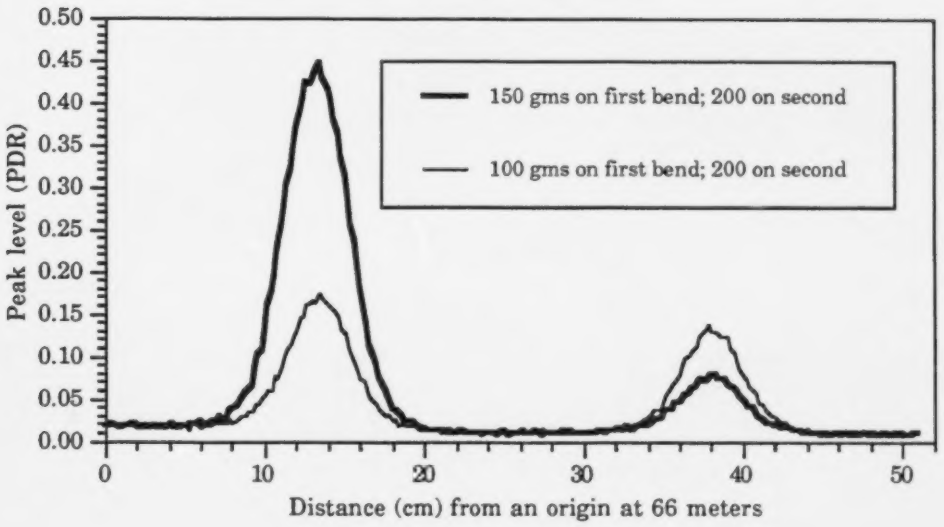

Figure 7.34 The effect on the backscattered trace after a force chang at one location.

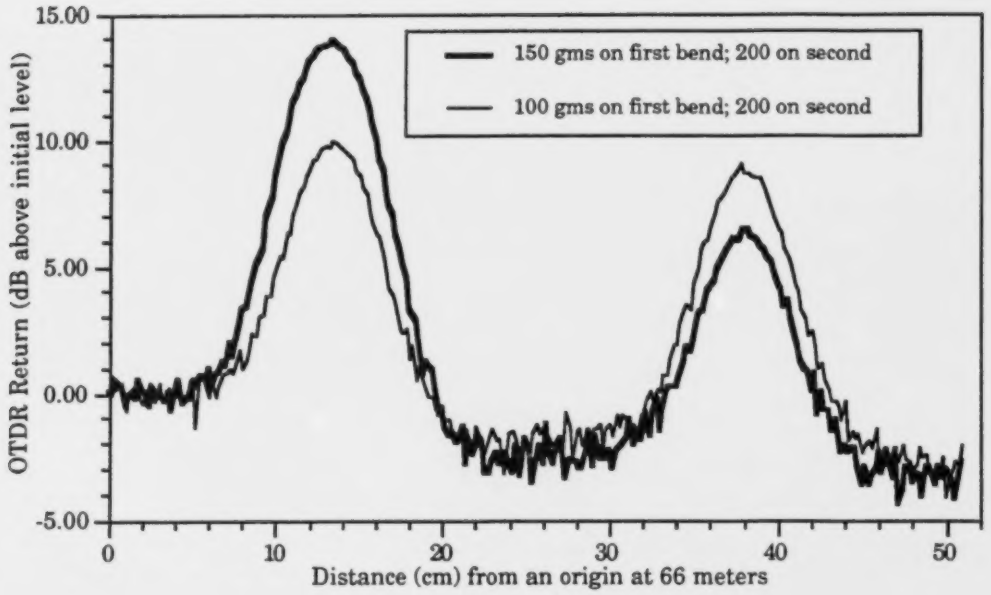

Figure 7.35 The backscattered trace expressed in decibels above or below the initial level.

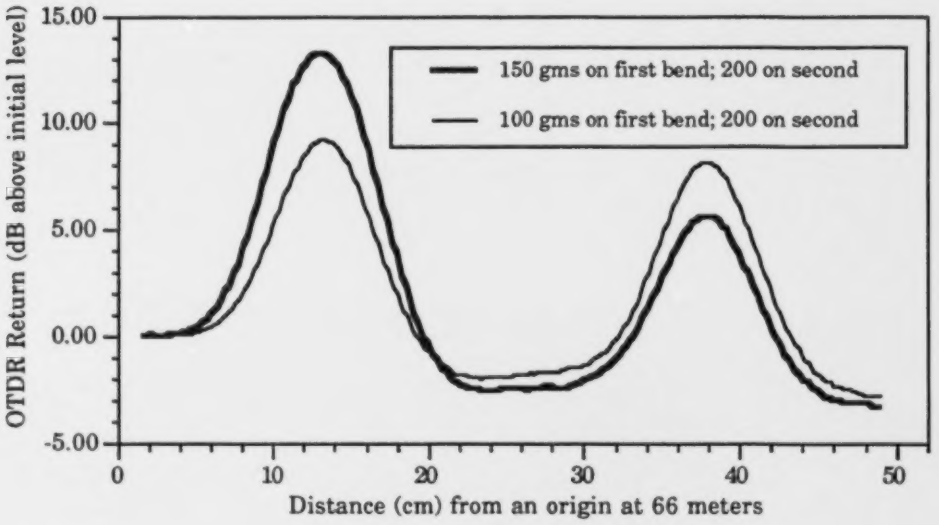

Figure 7.36 The smoothed backscattered trace.

Chapter 8

CONCLUSIONS

This project has established a connection between the profile of a bend and the enhancement in backscattering. Experimental evidence has strengthened our hypothesis that the backscattering enhancement originates from the recapture of light radiated at a bend. The jacket of the fibre has been found to be the main contributor to the enhanced backscatering. By removing the jacket, it has also been found that a layer of scattering particles surrounding the fibre is capable of producing similar enhancements of the backscattered trace.

A definite conclusion cannot be made that the jacket material causes all the additional backscattering. When a diffuse scatterer is in the vicinity of the bend region, there may be at least two additive components to the backscatter enhancement: the fibre jacket and the scatterer. The contribution of the diffuse scatterer can be separated if we can coat the fibre with a material that absorbs all radiated light escaping from the jacket. If further investigation proves the contribution from the external scattering medium to be significant and independently detectable, it will open possibilities for monitoring fibre optic cables by coating the fibre jacket with a scattering material. The location and severity of any potentially damaging bend in the cable can be detected by monitoring the fibre for signs of enhanced backscattering. If the scattering property of the medium can be modulated by electromagnetic fields, radiation or chemicals, a wide range of inexpensive distributed sensors may be developed for industrial use.

Since this research work was completed in June, 1990, a study has been published proposing a 'retro-reflection' transducer to make a larger number of serial elements possible[42]. In this transducer, the fibre is bent around a cylinder and placed near a reflecting material with index matching fluid in between. The reflecting material, composed of glass microspheres placed in metallic cavities, allows a fraction of the radiated light from the bend to reflect back into the fiber. It was shown that the light level due to this 'retro-reflection' is much larger than the Rayleigh backscattered light. Loss calculations showed that 10 to 20 sensors could be serially placed. Modulation of the reflected light is achieved by moving the reflecting surface. Springs and spacers are required to control the initial position and travel of the reflecting surface. Two splices are also required for each transducer. These considerations make this method of backscatter enhancement less advantageous in fully distributed sensing.

We achieved backscattering enhancement from a standard communications fibre operating at 850 nm wavelength with a commercially available OTDR equipment. The level of the peaks of the enhanced backscattering approached 15 dB above the level due to Rayleigh backscattering before the bend region. Thus, backscattering enhancement can be used to provide extra range for traditional microbending sensors, or better still, newer kind of sensor elements may be designed to produce detectable peak levels for very low transmission losses. Many such sensor elements can be serially connected to make practical distributed optical fibre sensors with ten or more elements active simultaneously. The total number of sensors that can be connected in series can be increased if

sensor elements are designed for extremely low loss when not activated. By suitable design, a truly continuous distributed sensor might be possible.

A photon counting OTDR is necessary to fully utilize the range of improvements possible through the method of backscattering enhancement proposed here. However, it is necessary to establish an accurate and stable relationship between the actual mean power level arriving at the photon counter and the photon detection ratio. The bias voltage of the avalanche photodiode should be stabilized so that the quantum efficiency of the reverse biased photodiode does not vary more than a few parts per thousand. It is also necessary to determine this quantum efficiency to relate the photon detection ratio to the average power arriving from a location. The optical fibre on an elastic foundation, and the area of contact between a fibre and a small diameter rod, needs to be studied from a mechanical view point.

Periodic microbending sensors have been the predominant sensor for the measurement of physical parameters such as force, displacement, and pressure at any one location in an optical fibre. The single bend enhanced backscattering sensor promises to be a viable alternative for simultaneous sensing at multiple locations.

Chapter 9

BIBLIOGRAPHY

1 J. Dakin, "Multiplexed and distributed optical fibre sensor systems," in *The Distributed Fibre Optic Sensing Handbook*, Edited by J. Dakin, IFS Publications, UK, Springer-Verlag, (1990) 3-19.

2 A. Rogers, "Distributed optical fibre sensors for the measurement of pressure, strain and temperature," in *The Distributed Fibre Optic Sensing Handbook*, Edited by J. Dakin, IFS Publications, UK, Springer-Verlag, (1990) 59-72.

3 A. Mickelson, O. Klevhus, and M. Eriksrud, "Backscatter readout from serial microbending sensors," Journal of Lightwave Technology, LT-2 (1984) 700-709.

4 A. De Jongh, M. Diemeer, E. Trommel, A. Breuls, "Simple fibre-optic sensor for detecting water penetration into optical fibre cables," Electronics Letters, 19 (1983) 980-982.

5 M. Diemeer and E. Trommel, "Fiber-optic microbend sensors: sensitivity as a function of distortion wavelength," Optics Letters, 9 (1984) 260-262.

6 N. Lagakos and J. Bucaro, "Optimizing fiber optic microbend sensor," Fiber Optic and Laser Sensors, 718 (1986) 12-20.

7 D. Marvin and N. Ives, "Wide-range fiber-optic strain sensor," Applied Optics, 23 (1984) 4212-4217.

8 N. Lagakos, J. Cole, and J. Bucaro, "Microbend fiber-optic sensor," Applied Optics, 26 (1987) 2171-2179.

9 C. Asawa, S. Yao, R. Stearns, N. Mota, J. Downs, "High-sensitivity fibre-optic strain sensors for measuring structural distortion," Electronics Letters, 18 (1982) 362-364.

10 B. Garside, "Ultrahigh resolution optical time-domain reflectometry," Opto-Electronics Inc., Oakville, ON, Canada, (1990), and private communication.

11 A. Cherin, *An Introduction to Optical Fibers*, McGraw-Hill, Toronto, ON, Canada, (1983).

12 R. Olshansky, "Propagation in glass optical waveguides," Reviews of Modern Physics, 51 (1979) 341-367.

13 C. Lin, *Optoelectronic Technology and Lightwave Communications Systems*, Van Nostrand Reinhold, New York, USA. 1989.

14 M. Eriksrud, A. Mickelson, and S. Lauritzen, "Backscattering signatures from optical fibers with differential mode attenuation," Journal of Lightwave Technology, LT-2 (1984) 139-145.

15 A. Mickelson and M. Eriksrud, "Theory of the backscattering process in multimode optical fibers," Applied Optics, 21 (1982) 1898-1909.

16 Technical Staff of CSELT, *Fiber Optic Communication Handbook*, Ed. F. Tosco, TAB Professional and Reference Books, Blue Ridge Summit, PA, U.S.A., 2nd Ed. (1990) 286-320.

17 L. Wood and F. Romero-Borja, "Attenuation by periodic micro-distortions of a sensor fiber," Optics Letters, 10 (1985) 630, 633-634.

18 M. Rourke, "Measurement of the insertion loss of a single microbend," Optics Letters, 6 (1981) 440-442.

19 J. Fields, "Attenuation of a parabolic-index fiber with periodic bends," Applied Physics Letters, 36 (1980) 799-801.

20 D. Marcuse, *Principles of Optical Fiber Measurements*, Academic Press, Toronto, (1981) 44 - 53.

21 D. Pinnow, T. Rich, F. Ostermayer, and M. DiDomenico, Jr, "Fundamental optical attenuation limits in the liquid and glassy state with application to fiber optical waveguide materials," Applied Physics Letters, 22 (1973) 527-528.

22 *Encyclopedia of Physics*, 3rd Edition, Van Nostrand, New York, USA, (1980) 905.

23 *American Institute of Physics Handbook*, 3rd Edition, McGraw Hill, New York, USA, (1972) 183.

24 F. Allard, *Fiber Optics Handbook For Engineers and Scientists*, McGraw-Hill, Toronto, ON, Canada. (1990).

25 *Polymer Science: A Materials Science Handbook*, North-Holland Publishing Company, Edited by A. Jenkins, 1 (1972) 234-247, 496-499, 528-529.

26 Product Information, Corguide® Optical Fiber, Telecommunications Products Division, Corning Glass Works, Corning, NY 14831, USA. 1 (1989) 1-3.

27 S. Personick, "Photon probe – an optical fiber time domain reflectometer," Bell Systems Technical Journal, 56 (1977) 355-366.

28 M. Rourke, "An overview of optical time-domain reflectometry," in Physics of Fiber Optics: Advances in Ceramics, The American Ceramic Society, Edited by B. Bendow and S. Mitra, 2 (1981) 252-277.

29 P. Healey, "Optical time domain reflectometry - a performance comparison of the analogue and photon counting techniques," Optical and Quantum Electronics, 16 (1984) 267-276.

30 S. Yukon, "Theory of optical time-domain reflectometry from perturbed fibers," in Physics of Fiber Optics: Advances in Ceramics, The American Ceramic Society, Edited by B. Bendow and S. Mitra, 2 (1981) 278-294.

31 Operating Manual, Picosecond Fiber Optic System, Opto-Electronics Inc., Oakville, ON, Canada. 1988.

32 M. Mitsuhiro and T. Horiguchi, "Advances in optical time-domain reflectometry," Journal of Lightwave Technology, 7 (1989) 1217-1224.

33 R. McIntyre, "The distribution of gains in uniformly multiplying avalanche photodiodes: theory," IEEE Transactions on Electron Devices, 19 (1972) 703-712.

34 R. McIntyre, "On the avalanche initiation probability of avalanche diodes above the breakdoen voltage," IEEE Transactions on Electron Devices, 20 (1973) 637-641.

35 J. Conradi, "The distribution of gains in uniformly multiplying avalanche photodiodes: experimental," IEEE Transactions on Electron Devices, 19 (1972) 713-718.

36 M. Barnoski, M. Rourke, S. Jensen, and R. Melville, "Optical time domain reflectometer," Applied Optics, 16 (1977) 2375-2379.

37 Operating Manual, Millimeter Resolution OTDR System, Opto-Electronics Inc., Oakville, ON, Canada. 1988.

38 G. Oscroft, "Intrinsic fibre optic sensors," Journal of Optical Sensors, 2 (1987) 269-279.

39 H. Taylor, "Bending effects in optical fibers,"Journal of Lightwave Technology, LT-2 (1984) 617-628.

40 K. Nagano, S. Kawakami, and S. Nishida, "Change of the refractive index in an optical fiber due to external forces," Applied Optics, 17 (1978) 2080-2085.

41 P. Gianino, and B. Bendow, "Calculations of stress-induced changes in the transverse refractive-index profile of optical fibers," Applied Optics, 20 (1981) 430-434.

42 F. Desforges, P. Graindorge, L. Jeunhomme, and H. Arditty, "Progress in optical time domain reflectometry: optical fibre sensor networks," The Distributed Fibre Optic Sensing Handbook, Edited by J. Dakin, IFS Publications, UK, Springer-Verlag, (1990) 95-101.